Impact of stratospheric aerosol intervention geoengineering on surface air temperature in China: A surface energy budget perspective

Zhaochen Liu[1, 4], Xianmei Lang[1, 2, 3], and Dabang Jiang[1, 3, 4*]

[1]Institute of Atmospheric Physics, Chinese Academy of Sciences, Beijing 100029, China
[2]Collaborative Innovation Center on Forecast and Evaluation of Meteorological Disasters, Nanjing University of Information Science and Technology, Nanjing 210044, China
[3]CAS Center for Excellence in Tibetan Plateau Earth Sciences, Beijing 100101, China
[4]College of Earth and Planetary Sciences, University of Chinese Academy of Sciences, Beijing 100049, China

Correspondence to: Dabang Jiang (jiangdb@mail.iap.ac.cn)

Abstract. Stratospheric aerosol intervention (SAI) geoengineering is a ~~rapid, effective, and promising means~~proposed scheme to counteract anthropogenic global warming, but the climate response to SAI, with great regional disparities, remains uncertain. In this study, we use Geoengineering Model Intercomparison Project G4 experiment simulations from ~~three~~six models ~~(HadGEM2-ES, MIROC-ESM, and MIROC-ESM-CHEM)~~ that ~~offset~~counteract anthropogenic forcing under medium-low emissions (RCP4.5) by injecting a certain amount of SO_2 into the stratosphere every year, to investigate the surface air temperature response to SAI geoengineering over China. ~~It has been shown~~We have found that ~~the~~ SAI leads to surface cooling over China ~~over~~during the last 40 years of injection simulation (2030–2069), which varies among models, regions and seasons. ~~The spatial pattern of SAI-induced~~Decreased tropospheric temperature ~~changes over China is mainly due to net surface~~ and water vapor and increased stratospheric aerosols induce robust decreases in downward clear-sky longwave and shortwave radiation ~~changes.~~fluxes at the surface respectively, dominating the temperature change over China. Changes in cloud effective forcing and surface albedo feedback also relate to the temperature response, but with large spatial and seasonal variations. We find that ~~changes in solar radiation modification strength, surface albedo, atmospheric water vapor and cloudiness affect surface shortwave radiation. In~~the increased summer~~, the increased~~ cloud cover ~~in some regions reduces net~~and winter surface albedo lead to strong cooling, while the decreased summer cloud cover and winter surface ~~shortwave radiation, causing strong surface cooling. In winter, both the strong~~albedo lead to weak cooling ~~in all three models and the abnormal~~or even warming ~~in MIROC-ESM are related to surface albedo changes.~~for the certain subregions and models. Our results suggest that cloud and land surface processes in models ~~may~~ dominate the spatial pattern of SAI-induced surface air temperature ~~changes~~change over China.

1 Introduction

The increasing anthropogenic greenhouse gas (GHG) concentrations since the industrial revolution have led to global warming. Although the international community has realized the risk of global warming and attempted to reduce GHG emissions, global GHG emissions still show a continuous increase (United Nations Environment Programme, 2020). The “2°C global temperature target” in the Paris Agreements will be unachievable if the current increasing emission trend persists

(e.g., Robiou du Pont and Meinshausen 2018). ~~Geoengineering, which aims to counteract global warming by deliberately changing the climate system, is therefore of great research interest. Geoengineering schemes are generally classified into two major types: carbon dioxide removal (CDR) geoengineering by reducing atmospheric carbon dioxide concentration, and solar radiation modification (SRM) geoengineering by increasing planetary albedo.~~Solar radiation modification (SRM), which refers to a range of measures adjusting the Earth's radiative balance, is considered as an option to counteract anthropogenic global warming. Various specific techniques have been proposed to perform SRM geoengineering, such as injecting sulfate aerosols into the stratosphere (Budyko, 1977), placing shields or deflectors in space (Seifritz, 1989), brightening marine clouds (Latham, 1990), and thinning cirrus clouds (Mitchell and Finnegan, 2009). The method of injecting sulfate aerosols or their precursors into the stratosphere, also known as stratospheric aerosol intervention (SAI) geoengineering, is designed to cool the surface by using these aerosols to reflect and scatter solar radiation (Crutzen, 2006; Wigley, 2006). As a proposed scheme, SAI has attracted great attention recently due to its assumed technological feasibility (e.g., Irvine et al., 2016).~~SAI geoengineering is considered the most promising SRM method due to its high effectiveness, affordability, and timeliness (Shepherd et al., 2009).~~

SRM geoengineering has not been implemented in reality because of its potential risks and immature technology. The primary means of recognizing the climate response to geoengineering is ~~by~~ simulating via general circulation models (GCMs). However, the results from early simulations could not be proved robust due to the differences in experimental schemes. The Geoengineering Model Intercomparison Project (GeoMIP) has been proposed to address that issue (Kravitz et al., 2011; 2015). To date, the GeoMIP has designed 12 experiments, including solar dimming, stratospheric aerosol intervention, marine cloud brightening, and cirrus thinning geoengineering in Coupled Model Intercomparison Project Phases 5 and 6 (CMIP5 and CMIP6). The GeoMIP provides detailed ~~simulating~~ guidelines for each model and experiment and calls for all the modeling groups worldwide to become involved and share their simulations. A total of 19 GCMs have participated in the GeoMIP to date. More detailed information is accessible from the GeoMIP website (http://climate.envsci.rutgers.edu/GeoMIP/).

Previous studies have indicated that SRM geoengineering could counteract or even reverse anthropogenic global warming and reduce sea ice melting and thermosteric sea-level rise, as well as

~~the~~ decreas~~cing~~ the frequency and intensity of extreme temperature and precipitation events (Rasch et al., 2008; Robock et al., 2015; Irvine et al., 2016; Ji et al., 2018; Jones et al., 2018). It ~~would~~might also come with risks. ~~First~~For instance, SRM geoengineering would reduce~~s~~ the global mean precipitation and monsoon precipitation and slow~~s~~ the hydrological cycle if it is used to offset the GHG-induced global warming (Bala et al., 2008; Tilmes et al., 2013; Sun et al., 2020). SRM would not mitigate the continued ocean acidification caused by CO_2 emissions (Caldeira et al., 2013).~~Second, SRM geoengineering might induce overcooling of the tropics and undercooling of the poles, which is related to the difference between the solar and CO_2 forcings (Russotto and Ackerman, 2018). Finally, t~~The sudden termination of geoengineering would lead to a more rapid increase in temperature than the non-geoengineered case (Matthews and Caldeira, 2007; Jones et al., 2013). ~~Moreover, for SAI geoengineering, the resultant cooling and enhanced polar vortex~~ The severity of the termination effect depends on the magnitude of geoengineering deployment. Moreover, the SAI-induced heterogeneous chemistry changes might cause stratospheric ozone depletion and thus increase ultraviolet radiation (UV) at the surface (Tilmes et al., 2008; Eastham et al., 2018).

The appropriate SRM geoengineering ~~could~~might lead to global cooling~~, but its regional effects might be different mainly due to the spatially heterogeneous reduction in solar radiation. This means~~ and benefit most regions (Irvine et al., 2019). However, it was still a concern that ~~if SRM geoengineering was performed,~~ some regions might face greater climatic impacts or risks ~~than others~~under SRM forcing (Ricke et al., 2013; Kravitz et al., 2014). For example, Robock et al. (2008) indicated that the ~~SAI-induced~~ weakening of the Asian and African summer monsoons caused by the injected stratospheric aerosols over the Arctic would decrease cloudiness and in turn warm the surface over northern Africa and India. In addition to the effect of cloudiness, changes in atmospheric moisture and surface conditions caused by SAI also impact surface air temperature (Kashimura et al., 2017). As the largest developing country in the world, China plays an important role in combating climate change. China's attitude to SAI is crucial to the international geoengineering research community. Considering the combined effect of the Tibetan Plateau and the East Asian monsoon, the climate over China would be strongly influenced by SAI. Large volcanic eruptions, which inject massive volcanic aerosols into the stratosphere, are considered a natural analog to SAI geoengineering (Trenberth and Dai, 2007). ~~For instance, the~~The 1815 Mt. Tambora eruption led to the "year without a summer" over China (e.g., Raible et al., 2016). ~~However,~~But the volcanic eruption is not a perfect analog. This is because the

sulfate aerosols from massive volcanic eruptions only last for 2–3 years, while the SAI-induced aerosols are continuously replenished for decades or centuries (Duan et al., 2019). So far, few studies have studied the temperature response to ~~the~~ SAI geoengineering over China ~~has not yet been studied~~ explicitly (Cao et al., 2015).

In this study, we investigate the impact of the SAI geoengineering on the surface air temperature over China and the underlying physical processes from a surface energy perspective. Section 2 provides a brief introduction to the experiments, model data, and decomposition method of ~~net~~ surface ~~shortwave radiation~~air temperature change. Section 3 evaluates the ability of models to reproduce the climatological temperature over China in summer and winter. Section 4 presents the summer and winter temperature changes and associated reasons over China in response to SAI geoengineering, and we also analyze the physical processes responsible for the SAI-induced ~~net surface shortwave radiation~~temperature changes over China. Conclusions and discussion are presented in Sect. 5.

2 Experiments, data, and methods

2.1 Experiments

We use the ~~simulations in the~~ G4 experiment from the first phase of the GeoMIP~~.~~ (Kravitz et al., 2011). As a SAI-based geoengineering experiment, G4 is designed to inject SO_2 into the low-level equatorial stratosphere at a consistent rate of 5 Tg per year under the background scenario of Representative Concentration Pathway 4.5 (RCP4.5) (Taylor et al., 2012). This injection rate is equivalent to a case in which the 1991 Mt. Pinatubo eruption occurred every four years (Bluth et al., 1992). The injection period is from 2020 to 2069, and then the experiment continues to run until 2089 to examine the termination effect (Jones et al., 2013). The RCP4.5 simulation for the same period is used as a baseline (non-geoengineered) state. In addition, the historical simulation for 1986–2005 is applied to evaluate the ability of the selected models to reproduce the climatology of surface air temperature over China.

2.2 Data

A total of ~~nine~~12 GCMs participated in the G4 experiment~~, and four of them are available on the~~

~~Earth System Grid Federation (ESGF), including CSIRO-Mk3L-1-2, HadGEM2-ES, MIROC-ESM, and MIROC-ESM-CHEM~~ (Kravitz et al., 2013a). However, some models should not be considered in this study due to their known issues. For instance, CSIRO-Mk3L-1-2 runs G4 by directly reducing solar irradiance rather than injecting stratospheric aerosols; GISS-E2-R shows an inconsistency between G4/RCP4.5 and historical experiments; IPSL-CM5A-LR and NorESM1-M have errors in the longwave treatment of the sulfate aerosol; GEOSCCM and ULAQ use prescribed sea surface temperatures.~~Note that CSIRO-Mk3L-1-2 is not selected because the clear-sky shortwave radiation flux at the surface is not available in its outputs (Phipps et al., 2011).~~ Simulations from the other ~~three~~six models are applied for analyses. Monthly datasets are used and calculated as the averages in summer (June–July–August, JJA) and winter (December–January–February, DJF). ~~Considering the intermodel scatter in the temperature response to SAI in the G4 experiment, we analyze the results of each model separately (Yu et al., 2015; Ji et al., 2018).~~ The CN05.1 observation dataset (Wu and Gao, 2013) is used to evaluate the ability of models to reproduce the climatology of temperature over China. All the observations and model outputs are interpolated to a common grid with a mid-range horizontal resolution (2.5° longitude by 2° latitude).

A brief description of the selected models ~~used~~ is illustrated in Table 1. In addition to differences in the physical and chemical modules related to sulfate aerosol particles, the models have different SO_2 injection treatments. For HadGEM2-ES, the CLASSIC aerosol module (Bellouin et al., 2011) used in the stratosphere makes it possible to handle the injections of SO_2, allowing HadGEM2-ES to finish a complete simulation including the generation and transportation of stratospheric sulfate aerosols. The injection point is located on the equator (0° longitude), and the injection altitude ranges from 16 to 25 km. For CanESM2, the stratospheric aerosol optical depth (SAOD) caused by SAI is prescribed as a consistent value. For other models (BNU-ESM, CNRM-ESM1, MIROC-ESM and MIROC-ESM-CHEM~~, the SPRINTARS aerosol module mainly focuses on tropospheric aerosols. The~~), the prescribed distribution of ~~stratospheric sulfate aerosol optical depth (AOD),~~SAOD, according to Sato (2006), is used to drive the G4 experiment. ~~The only difference between MIROC-ESM and~~Besides, MIROC-ESM-CHEM ~~is that the latter is coupled with the CHASER atmospheric chemistry module, which can be used to calculate~~calculates the surface density of sulfate aerosols by using the CHASER atmospheric chemistry module (Sudo et al., 2002; Kravitz et al., 2013a).

2.3 Decomposition method for SAI-induced ~~shortwave radiation changes at the surface~~surface air temperature change

~~The surface air temperature change depends on the components of the surface energy budget, including shortwave and longwave radiation (SW and LW) and sensible and latent heat (SH and LH) (Boer, 1993). For example, the surface radiation (SW and LW) changes due to SRM geoengineering may be balanced by the surface temperature and/or nonradiative (SH and LH) flux changes (Andrew et al., 2009). Previous studies indicated that SRM geoengineering could reduce the surface SW, which was mainly compensated by the decreased LH flux (e.g., Schmidt et al., 2012). Therefore, it is important to analyze the surface SW response to SAI forcing in this study.~~

Surface air temperature is a widely used variable in climate studies. Change in surface air temperature is associated with three components: surface vertical energy fluxes (including radiative and heat fluxes), horizontal temperature advection, and adiabatic warming or cooling (Gong et al., 2017). In this study, the SAI-induced changes in surface temperature and surface air temperature are strongly coupled in China during 2030–2069 (the correlation coefficients are higher than 0.98 and 0.99 in summer and winter, respectively; Fig. 1). Thus, the surface vertical energy fluxes are considered to be the main factor affecting temperature change under SAI forcing.

According to the decomposition method based on the surface energy budget proposed by Lu and Cai (2009), the surface air temperature change caused by SAI can be written as:

$$\Delta T = \frac{\Delta R^{\downarrow} + \Delta \mathrm{LH} + \Delta \mathrm{SH} + \Delta Q}{4\sigma \overline{T_s}^3} + \mathrm{Res} \quad (1)$$

~~A decomposition method for the SAI-induced net surface SW changes proposed by Kashimura et al. (2017) is applied for this study. That method is based on the single-layer atmospheric model of SW transfer according to Donohoe and Battisti (2011) which assumes that the transportation processes of SW, including atmospheric reflection, atmospheric absorption, and surface reflection, are isotropic. As detailed by Kashimura et al. (2017), the upward SW at the top of the atmosphere (TOA) and the upward and downward SW at the surface at each grid point can be approximated as:~~

~~$$\mathrm{SW}^{\uparrow}_{\mathrm{TOA}} = SR + S\alpha \frac{(1-R-A)^2}{1-\alpha R} \quad (1)$$~~

~~$SW^{\downarrow}_{SURF} - S\frac{(1-R-A)}{1-\alpha R}$ (2)~~

~~$SW^{\uparrow}_{SURF} - \alpha SW^{\downarrow}_{SURF} - \alpha S\frac{(1-R-A)}{1-\alpha R}$ (3)~~

where Δ represents the difference between G4 and RCP4.5, the overbar represents the climatological value of RCP4.5, $R^{\downarrow}$ is the downward net radiation at the surface, LH and SH are surface sensible and latent heat fluxes respectively, Q is surface heat storage, T_s is surface temperature, and σ is the Stefan-Boltzmann constant. Res represents the difference between changes in surface air temperature and surface temperature. In order to quantitatively separate the radiative effects of clouds and surface albedo, the $\Delta R^{\downarrow}$ can be decomposed as follow:

~~where S is the downward SW at the TOA ($SW^{\downarrow}_{TOA}$), R is the fraction of reflection, A is the fraction of absorption during SW passing through the atmosphere, and α is the surface albedo. Considering that the four components of SW flux above (S, $SW^{\uparrow}_{TOA}$, $SW^{\downarrow}_{SURF}$ and $SW^{\uparrow}_{SURF}$) are directly available from model outputs, R, A, and α can be calculated from Eqs. (1)–(3) as follows:~~

~~$R = \frac{S \cdot SW^{\uparrow}_{TOA} - SW^{\downarrow}_{SURF} SW^{\uparrow}_{SURF}}{S^2 - SW^{\uparrow 2}_{SURF}}$ (4)~~

~~$A = (1-R) - \frac{SW^{\downarrow}_{SURF}}{S}(1-\alpha R)$ (5)~~

~~$\alpha = \frac{SW^{\uparrow}_{SURF}}{SW^{\downarrow}_{SURF}}$ (6)~~

$$\Delta R^{\downarrow} = \Delta LW^{cs\downarrow} + (1-\overline{\alpha})\Delta SW^{cs\downarrow} + \Delta SAF + \Delta CRF \quad (2)$$

$$\Delta SAF = -(\Delta SW^{as\downarrow} + \overline{SW^{as\downarrow}})\Delta\alpha \quad (3)$$

$$\Delta CRF = (1-\overline{\alpha})\Delta SW^{cl\downarrow} + \Delta LW^{cl\downarrow} \quad (4)$$

In Eqs. (2)–(4), $SW^{as\downarrow}$ represents downward surface shortwave radiation in all-sky conditions, $SW^{cs\downarrow}$ and $LW^{cs\downarrow}$ represent downward surface shortwave and longwave radiations in clear-sky conditions respectively, $SW^{cl\downarrow}$ and $LW^{cl\downarrow}$ represent downward shortwave and longwave radiative effects of clouds (all-sky radiations minus clear-sky radiations) respectively, and α represents surface albedo (the ratio of solar radiation reflected to the atmosphere at the surface). SAF is surface albedo feedback, and CRF is cloud radiative forcing. Under SAI forcing, both the changes in atmospheric

reflection and atmospheric absorption affect the $SW^{cs\downarrow}$. We assume that the clear-sky atmospheric reflection change is only affected by atmospheric water vapor amount, and the clear-sky atmospheric absorption change is only affected by the aerosol scattering effect. As detailed by Kashimura et al. (2017), the change in $SW^{cs\downarrow}$ can be further decomposed as:

~~It is noticeable that both R and A are affected by cloud cover. That is, both of them are all-sky values (R^{as} and A^{as}). The clear-sky values of R and A (R^{es} and A^{es}) are calculated using the clear-sky values of $SW^{\uparrow}_{TOA}$, $SW^{\downarrow}_{SURF}$ and $SW^{\uparrow}_{SURF}$ to separate the effect of clouds. The effect of clouds, which is denoted as "cl", is calculated from the difference between all-sky and clear-sky values (e.g., $R^{cl} \equiv R^{as} - R^{cs}$). In addition, we assume that the impact of clouds on surface albedo (α) is negligible. The values of surface albedo are uniformly calculated using the all-sky values of SW collected at the surface in this study. Here, the flux is defined as downward positive, and the net surface SW at each grid point can be represented as a function of S, R^{as}, A^{as}, R^{es}, A^{es}, and α as follows:~~

~~$$SW^{net}_{SURF} = SW^{\downarrow}_{SURF} - SW^{\uparrow}_{SURF}$$~~

~~$$= (1-\alpha) S \left[\frac{1-(R^{cs}+R^{cl})-(A^{cs}+A^{cl})}{1-\alpha(R^{cs}+R^{cl})} \right] \quad (7)$$~~

~~As shown in Fig. 1, the effects of SAI on the net surface SW can be divided into four parts: effects of changes in the strength of solar radiation modification (SW_{SRM}), amount of atmospheric water vapor (SW_{WV}), cloud cover (SW_C), and surface albedo (SW_{SA}). Here we further assume that the changes in solar radiation modification strength and water vapor amount would only lead to changes in R^{es} and A^{es} respectively, and the concentrations of other atmospheric compositions related to R^{es} and A^{es} would not be affected by SAI. The net surface SW change can therefore be decomposed as follows:~~

~~$$SW_{SRM} \equiv SW^{net}_{SURF}(S, R^{cs}_{G4}, R^{cl}_{RCP}, A^{cs}_{RCP}, A^{cl}_{RCP}, \alpha_{RCP}) - SW^{net}_{SURF}(RCP) \quad (8)$$~~

~~$$SW_{WV} \equiv SW^{net}_{SURF}(S, R^{cs}_{RCP}, R^{cl}_{RCP}, A^{cs}_{G4}, A^{cl}_{RCP}, \alpha_{RCP}) - SW^{net}_{SURF}(RCP) \quad (9)$$~~

~~$$SW_{C} \equiv SW^{net}_{SURF}(S, R^{cs}_{RCP}, R^{cl}_{G4}, A^{cs}_{RCP}, A^{cl}_{G4}, \alpha_{RCP}) - SW^{net}_{SURF}(RCP) \quad (10)$$~~

~~$$SW_{SA} \equiv SW^{net}_{SURF}(S, R^{cs}_{RCP}, R^{cl}_{RCP}, A^{cs}_{RCP}, A^{cl}_{RCP}, \alpha_{G4}) - SW^{net}_{SURF}(RCP) \quad (11)$$~~

$$\Delta SW^{cs\downarrow} \approx \Delta SW_{SRM} + \Delta SW_{WV} \quad (5)$$

$$\Delta SW_{SRM} = SW^{cs\downarrow}(F^{cs}_{G4}, A^{cs}_{RCP}) - \overline{SW^{cs\downarrow}} \quad (6)$$

$$\Delta SW_{WV} = SW^{cs\downarrow}(F^{cs}_{RCP}, A^{cs}_{G4}) - \overline{SW^{cs\downarrow}} \quad (7)$$

where F is the fraction of solar radiation reflected by the atmosphere, and A is the fraction of absorption during solar radiation passing through the atmosphere. SW_{SRM} and SW_{WV} represent the effects of solar radiation scattering and atmospheric water vapor amount, respectively. Although the $SW^{cs\downarrow}$ change is not precisely equal to the sum of changes in SW_{SRM} and SW_{WV} due to the assumption of a single-layer model (Donohoe and Battisti, 2011), this method is effective when analyzing the surface shortwave radiation change in response to SAI (Kashimura et al., 2017).

~~Although the net surface SW differences between G4 and RCP4.5 are not precisely equal to the sum of SW_{SRM}, SW_{WV}, SW_C, and SW_{SA} changes due to the assumption of a single-layer model and the nonlinearity of Eq. (7), this method is effective when analyzing the net surface SW change in response to SAI geoengineering.~~

3 Evaluation of the models

The ability of the models to reproduce the surface air temperature over China is evaluated first. As shown in Fig. 2, the spatial correlation coefficient (SCC), standard deviation (SD), and centered root-mean-square error (CRMSE) between the observation and the historical simulation for ~~the~~ climatological temperature over China during 1986–2005 are calculated and illustrated in a Taylor diagram (Taylor, 2001). The SCCs of the models range from 0.~~88~~85 to 0.95 (0.94 in multi-model mean) in summer and from 0.91 to 0.96 (0.96 in multi-model mean) in winter. All the SCCs are statistically significant at the 99% level, meaning that the simulated temperature is in good agreement with the observed temperature. The normalized SDs range from 0.~~95~~81 to 1.~~07~~33 in summer (0.99 in multi-model mean) and from 1.~~07~~03 to 1.~~16~~23 (1.08 in multi-model mean) in winter. This result indicates that all ~~three~~selected models overestimate the spatial variability of the winter temperature ~~except for HadGEM2-ES~~ in ~~summer~~China. The CRMSEs are 0.~~31–0.51~~34–0.53 (0.35 in multi-model mean) for summer and 0.~~33~~32–0.46 (0.31 in multi-model mean) for winter. Taken together, the simulations of summer and winter temperatures by selected models are reliable over China. ~~HadGEM2-ES performs better than MIROC-based models, which may be related to its finer horizontal resolution.~~ The multi-model mean results outperform most individual models for the temperature climatology over China both in summer and winter, which is consistent with previous

findings (e.g., Jiang et al., 2016).

The observed spatial ~~distributions~~patterns of summer and winter temperature ~~biases~~climatology over China ~~between simulations~~show a general decrease from south to north, and ~~observations are shown~~the lowest values mainly occur in ~~Fig. 3.~~the Tibetan Plateau (Figs. 3a, d). These features can be well reproduced by all models and their mean (Figs. 3b, e). Compared to the ~~observations,~~observation, the simulated temperature is generally overestimated in summer but underestimated in winter over China according to the regionally averaged values. ~~In MIROC-ESM and MIROC-ESM-CHEM, cold biases mainly occur over the Tibetan Plateau, and~~ In summer, warm biases ~~mainly~~ occur in ~~Xinjiang Province in both summer and winter. The spatial variations~~most of ~~the temperature biases in HadGEM2-ES are relatively small relative to those in MIROC-based models. In summer, the temperature is overestimated over~~ eastern China, especially in northeastern China~~, northern Xinjiang, and the Tibetan Plateau, but underestimated over areas south of the Yangtze River in HadGEM2-ES (Fig. 3a).~~ (Fig. 3c). In winter, however, the ~~simulated~~underestimation of temperature ~~in HadGEM2-ES is generally lower than that observed over China~~exists at the national scale, with a regionally averaged cold bias of ~~−3.04~~1.79°C ~~(Fig. 3d).~~in multi-model mean (Fig. 3f). Substantial cold biases occur over the Tarim Basin and the Tibetan Plateau, which are associated with regional topography. Most of the above biases are consistent among individual models, with the averaged model consistency of 76% over China in both summer and winter.

4 Results

4.1 Changes in surface air temperature over China

~~Figure~~Figures 4 ~~shows~~and 5 show the temporal ~~evolutions~~evolution of surface air temperature changes in the G4 experiment and RCP4.5 scenario relative to the present climatology (1986–2005) over China. Both the summer and winter temperatures in G4 increase over time, although they are colder than those in RCP4.5. Positive values occur throughout the whole G4 simulation period, excluding ~~the first~~ several years in ~~HadGEM2-ES and MIROC-ESM. The cooling effect of~~ winter. This indicates that although the injection of 5 Tg SO_2 per year ~~cannot return~~leads to a surface cooling over China, the climatological temperature ~~over China under RCP4.5 to~~ in G4 is still higher than the

present level~~, but can delay warming for several years~~. Considering that the feedback response timescale of diffusive ocean heat uptake in climate models is approximately ten years (Jarvis, 2011), ~~simulations~~the simulation representing the last 40 years of injection (2030–2069) ~~are~~is used to examine the temperature response to SAI over China, as done by Kravitz et al. (2013b) and Tilmes et al. (2013). During this period, the warming trends over all of China in ~~the~~ G4 ~~experiment~~among models are 0.~~36~~21–0.~~42~~43°C decade^{-1} in summer and 0.~~35~~30–0.~~48~~59°C decade^{-1} in winter. ~~As shown in Fig. 4,~~ It can be seen that the warming trend ~~differences~~difference between G4 and RCP4.5 ~~are~~is small~~. This indicates that SAI in the G4 experiment has little impact on the warming~~, and this is expected because of the similar trend ~~over China caused by GHG concentrations when the climate system reaches a relatively stable state~~of radiative forcing variation in the two experiments during 2030–2069. The ~~changes in~~regionally averaged temperature over China ~~in G4 compared to RCP4.5 show that the strongest SAI-induced cooling occurs in HadGEM2-ES, with regional averages of~~ is decreased by 0.24–0.96°C (0.64°C in the multi-model mean) in summer and 0.30–1.52°C (0.80°C in the multi-model mean) in winter~~.~~ due to SAI forcing. Although the magnitude of SAI-induced temperature change varies across models and seasons, the cooling response is consistent among models over China. The ~~SAI-induced~~winter cooling ~~in winter~~ is ~~also~~ stronger than ~~that in~~the summer ~~in~~ level in all models. Additionally, the result shows the strongest SAI-induced cooling occurs in HadGEM2-ES in both~~MIROC-ESM-CHEM, with magnitudes of −0.61°C and −0.42°C, respectively. The cooling effect in winter (−0.56°C) is slightly weaker than that in~~ summer ~~(−0.60°C) in MIROC-ESM~~and winter.

The spatial ~~patterns~~pattern of the temperature ~~differences~~difference between G4 and RCP4.5 over China ~~are~~is illustrated in ~~Fig. 5~~Figs. 6 and 7. The multi-model results show a robust and coherent cooling in both summer and winter. Strong cooling with magnitudes greater than 0.8°C mainly occurs over high-latitude regions, including northwestern and central China. For the individual models, the SAI-induced temperature changes are negative and significant almost everywhere over China except for in MIROC-ESM and MIROC-ESM-CHEM. SAI leads to the temperature increases over the upper reaches of the Yellow River and the middle and upper reaches of the Yangtze River in MIROC-ESM in winter, and over northeastern and southeastern China in MIROC-ESM-CHEM in summer, respectively (Figs. 6f and 7e). These increases are weak and insignificant.~~In summer, SAI-induced temperature changes are negative everywhere over China in all three models (Fig. 5a–c). In HadGEM2-ES, strong cooling occurs in the Yangtze–Huaihe River Basin and northern Xinjiang with~~

~~magnitudes of −1.8 to −1.6°C (Fig. 5a). In MIROC-ESM and MIROC-ESM-CHEM, strong cooling with magnitudes of −1.1 to −0.8°C occurs in southeastern China and central Inner Mongolia, and the Tibetan Plateau, respectively (Fig. 5b–c). In winter, the cooling effect of SAI also occurs over all of China in HadGEM2-ES and MIROC-ESM-CHEM, with strong cooling over the Tibetan Plateau and northeastern China (up to −1.7°C), and northern China (up to −0.8°C), respectively (Fig. 5d–e). For MIROC-ESM, although SAI induces significant cooling over the southern Tibetan Plateau and northeastern China, its impact on winter temperature is weaker than −0.1°C and statistically insignificant in most of Central China. Moreover, the SAI induces slight warming over the source region of the Yellow River and the Sichuan Basin (Fig. 5f).~~ The physical processes responsible for SAI-induced cooling or warming will be discussed in the subsequent sections.

4.2 ~~Changes in surface energy components over China~~Decomposition of SAI-induced temperature change

We decompose the SAI-induced change in surface air temperature over China by utilizing Eqs. (1)–(4). The regionally averaged value of each term is illustrated in Fig. 8. It can be seen that SAI decreases downward net surface radiation fluxes, leading to a surface cooling of 0.30–1.45°C in summer and 0.48–2.10°C in winter over China. These decreases are partly compensated by decreased nonradiative fluxes, especially the decreased LH. The contributions of SH, Q, and Res are relatively small (Fig. 8a). The decomposition of downward surface radiation shows the decreases in $SW^{cs\downarrow}$ and $LW^{cs\downarrow}$ in all models. The reduced $LW^{cs\downarrow}$ dominates the deficient downward net surface radiation and decreases the temperature with magnitudes of 0.38–1.33°C in summer and 0.25–1.38°C in winter. The reduced $SW^{cs\downarrow}$ also contributes to the surface cooling, with magnitudes of 0.04–0.33°C in summer and 0.13–0.41°C in winter. The winter decrease in $SW^{cs\downarrow}$ is stronger than the summer one in most models. Besides, the inter-model differences in CRF and SAF changes are relatively substantial. The area-averaged results illustrate that the changes in CRF and SAF have negative and positive contributions to the SAI-induced cooling over China in most models, respectively (Fig. 8b).

The spatial patterns of SAI-induced changes in key energy-related variables over China are illustrated in Fig. 9. Under SAI forcing, changes in atmospheric temperature and water vapor lead to a general decrease in the $LW^{cs\downarrow}$. The $SW^{cs\downarrow}$, primarily related to the solar radiation scattering effect by stratospheric sulfate aerosol particles, also exhibits a coherent reduction over China. The spatial pattern

of temperature change over China is primarily determined by $SW^{cl\downarrow}$ and surface albedo changes. In summer, most models exhibit increases in cloud amount, especially over northwestern and central China. The resultant decreased $SW^{cl\downarrow}$ leads to strong cooling over these regions. Conversely, northeastern and southeastern China show increased $SW^{cl\downarrow}$ and relatively weak cooling (Fig. 9d). In MIROC-ESM-CHEM, the excessive $SW^{cl\downarrow}$ (up to 8 W m^{-2}) offsets the clear-sky radiative effects and causes abnormal warming over most regions of eastern China (Fig. S1a). In summer, the surface albedo change due to SAI over China is relatively small. The increased surface albedo mainly occurs in the Tibetan Plateau, which contributes to local surface cooling (Fig. 9f). This may help to explain why the cloud effect is not a primary factor of temperature change over the Tibetan Plateau in summer.

In winter, a robust and coherent SAI-induced reduction in cloud cover is found over China (Fig. 9k). This reduction leads to a general increase in $SW^{cl\downarrow}$, causing the weak cooling south of the Yangtze River valley. In other areas of China, however, the change in surface albedo is the primary factor affecting the spatial pattern of temperature response under SAI forcing. The increased surface albedo leads to strong cooling, especially over northwestern and central China. However, the decreased surface albedo is found over the upper reaches of the Yellow River and the middle and upper reaches of the Yangtze River in MIROC-ESM with magnitudes greater than 3%, which results in the abnormal winter warming mentioned above (Fig. S1d). Taken together, the increased summer cloud cover and winter surface albedo lead to strong cooling, while the decreased summer cloud cover and winter surface albedo result in weak cooling, or even warming for the certain subregions and models, for instance eastern China in MIROC-ESM-CHEM and the upper reaches of the Yellow River and the middle and upper reaches of the Yangtze River in MIROC-ESM.

~~We calculate the regional mean changes in surface air temperature, surface radiation, and surface turbulent heat fluxes due to SAI forcing over China (Fig. 6). A reduced net surface SW and an increased downward surface LH flux occur in all three models in both summer and winter, although their magnitudes vary. This indicates that the SAI-induced net surface SW deficit leads to surface cooling, while the deficient surface radiation is partly compensated by the increased downward LH flux over China. The decrease in clear-sky net surface SW (SW_CS), which is primarily related to the solar radiation scattering effect by stratospheric sulfate aerosol particles, is the main cause of the decreased SW. In contrast, the changes in the SW cloud radiative effect (SW_CRE) are positive and relatively small. Similarly, the decreased surface net LW contributes to surface cooling, excluding that occurred~~

in HadGEM2-ES in winter. The regionally averaged changes in LW_CS and LW_CRE exhibit a distinctive difference between summer and winter. The decreased net surface LW is caused by the negative changes in LW_CS in summer, but by the negative changes in LW_CRE in winter.

The spatial patterns of SAI-induced changes in key energy-related variables over China are illustrated in Fig. 7 and S1–S2. In summer, the changes in net surface SW over China are closely related to those in SW_CRE. The regionally averaged changes in the cloud cover fraction over China show a consistent increase in all three models, with magnitudes of 0.10% in HadGEM2-ES, 0.04% in MIROC-ESM, and 0.06% in MIROC-ESM-CHEM. The increase in cloud cover, which mainly occurs in the Yangtze-Huaihe River Basin and northern Xinjiang in HadGEM2-ES and southeastern China and central Inner Mongolia in MIROC-ESM, induces a decrease in SW_CRE, leading to a strong cooling over these regions. Additionally, the deficit of the downward LH flux, especially over the Yangtze-Huaihe River Basin in HadGEM2-ES and central Inner Mongolia in MIROC-ESM, can increase cloud cover and amplify cooling although the regional mean changes in LH are positive. For the MIROC-based models, the large positive values of SW_CRE changes over the Tibetan Plateau are counteracted by decreased SW_CS, inducing a strong cooling in MIROC-ESM-CHEM (Fig. S1b and S2b). In addition, the spatial patterns of the net surface LW differences over China between G4 and RCP4.5 are consistent with those of the net surface SW differences in both summer and winter, but with opposite signs. The changes in LW are mainly dominated by those in LW_CS. One possible explanation is that the strong surface cooling caused by decreased net surface SW increases upward surface LW, which is enough to counteract the SAI-induced deficit of downward surface LW, leading to the positive net surface LW change.

In winter, a uniform SAI-induced reduction in cloud cover is found over China, with regional averages of − 0.64% in HadGEM2-ES, − 0.69% in MIROC-ESM, and − 0.38% in MIROC-ESM-CHEM. This reduction leads to a general increase in the SW_CRE over China, causing the positive SW change south of the Yangtze River (Fig. 7k and S1k–S2k). In other areas of China, however, the changes in the net surface SW are closely related to SW_CS. The SAI-induced decrease in SW_CS leads to strong cooling over the Tibetan Plateau and northeastern China in HadGEM2-ES, northeastern China in MIROC-ESM, and northern China in MIROC-ESM-CHEM. Moreover, an increase in SW_CS is found over the source region of the Yellow River and the Sichuan Basin in MIROC-ESM with magnitudes greater than 6 W m^{-2}, leading to the abnormal winter warming mentioned above.

~~Altogether, the spatial pattern of SAI-induced temperature changes over China is mainly due to those in net surface SW. The deficit of net surface SW which leads to a strong surface cooling is mainly induced by the decreased SW_CRE in summer and the decreased SW_CS in winter. The exception is the strong surface cooling in summer over the Tibetan Plateau in MIROC-ESM-CHEM, which is related to the decreased SW_CS. In winter, abnormal warming is associated with a large positive SW_CS change in response to the SAI forcing.~~

4.3 Physical processes responsible for ~~the~~ SAI-induced ~~SW change.~~temperature changes

Previous studies have illustrated that the SAI reduces the tropospheric temperature and atmospheric water vapor amount on a global scale (Kashimura et al., 2017; Visioni et al., 2018). In China, these reductions cause the decreased $LW^{cs\downarrow}$, contributing to the surface cooling primarily. We further address the potential reasons for the $SW^{cs\downarrow}$ change by using the aforementioned decomposition method. The atmospheric reflection of solar radiation increases after sulfate aerosols injection. In our study, the effect of aerosols scattering on shortwave radiation is represented as SW_{SRM}, which can be measured by the change in SAOD. As shown in Fig. 10, the latitudinal distributions of the calculated (used in HadGEM2-ES) and prescribed (used in BNU-ESM, CNRM-ESM1 and the MIROC-based models) SAOD changes caused by SAI in G4 display a coherent increase over China. The distribution in CanESM2 is not shown because it is a constant field according to the experimental design. The SAOD change in HadGEM2-ES is unavailable. Total aerosol optical depth is therefore considered as a reasonable alternative variable for SAOD (e.g., Bellouin et al., 2011). The national-scale increased SAOD results in a robust decrease in SW_{SRM} (Figs. 11a, d), contributing to the surface cooling with magnitudes of 0.21–0.54°C in summer and 0.26–0.69°C in winter. Besides, the deficit in column-integrated water vapor reduces the atmospheric absorption of solar radiation. The resultant increased SW (SW_{WV}) counterbalance 37–81% and 11–48% of the reductions in SW_{SRM} over China in summer and winter, respectively (Figs. 11b, e). This is the main reason why the SAI-induced winter cooling is severer than the summer level.

~~Kashimura et al. (2017) pointed out that the net surface SW changes can at least explain a cooling of −1.1 to −0.2°C in response to the SAI forcing in the G4 experiment on a global scale. According to the above results, the spatial patterns of temperature differences over China between G4 and RCP4.5 are mainly determined by the net surface SW changes. The cloud radiative changes occurring over~~

~~China have been discussed above. In this section, we further address other potential reasons for net surface SW changes by using the aforementioned decomposition method. Spatial patterns and regionally averaged values of the decomposition results over China are illustrated in Fig. 8 and S3–S4. In response to the SAI forcing, changes in the solar radiation modification strength and surface albedo lead to a decrease in net surface SW (SW_{SRM} and SW_{SA}), while those in atmospheric water vapor and cloudiness lead to an increase in net surface SW (SW_{WV} and SW_{C}) over China in both summer and winter, although their magnitudes vary among models and seasons. Furthermore, the decrease in SW_{SRM} is the largest contributor to the decreased net surface SW over China in all models, with magnitudes of −2.01 to −1.21 W m^{-2} in summer and −3.00 to −1.13 W m^{-2} in winter.~~

As discussed in Sect. 4.2, the spatial patterns of summer and winter temperature changes over China are mainly determined by the $SW^{cl\downarrow}$ and surface albedo, respectively. Generally, the SAI-induced decrease in LH flux reduces the low cloud cover, resulting in the positive change in $SW^{cl\downarrow}$ (Figs. 11c, f). Through this process, the significantly decreased LH over northeastern and southeastern China causes the abnormal summer warming in MIROC-ESM-CHEM (Fig. S1c). However, in summer, the effect of LH is partly offset by the SAI-induced moisture convergence at the troposphere in most models. The resultant increased cloud cover enhances the surface cooling over northwestern and central China (Fig. 11h). The change in surface albedo is closely related to land surface conditions. The SAI-induced cooling can be amplified by increased snow cover or sea ice (e.g., Schmidt et al., 2012). Considering surface albedo can be reasonably described as a linear function of snow cover fraction (Qu and Hall, 2007; Li et al., 2016), we further investigate the spatial pattern of changes in snow cover fraction, and find that matches with surface albedo over China (Figs. 11i, l; note that model data are not available for HadGEM2-ES). Under SAI forcing, the increased snow cover mainly occurs over the Tibetan Plateau in summer, and over northwestern and central China in winter. The enlarged snow cover fraction gives rise to SW decrease at the surface, which in turn has a positive feedback on surface cooling. Furthermore, the SAI-induced abnormal winter warming in MIROC-ESM is also associated with the decreased snow cover over the upper reaches of the Yellow River and the middle and upper reaches of the Yangtze River (Fig. S1e).

~~The spatial distributions of the SAI-induced SW_{SRM} and SW_{WV} changes show a general decrease and increase across China, respectively (Fig. 8 and S3–S4). The latitudinal distributions of the calculated (used in HadGEM2-ES) and prescribed (used in MIROC-based models) stratospheric AOD~~

changes caused by SAI in the G4 experiment indicate a uniform increase in stratospheric AOD over China (Fig. 9). Note that the stratospheric AOD change in HadGEM2-ES is unavailable, and the tropospheric and stratospheric AOD change is therefore considered as a reasonable alternative (e.g., Bellouin et al., 2011). The increased AOD reflects the increased amount of stratospheric sulfate aerosol particles which leads to the decrease in the SW_{SRM}. The results also show that the calculated value of the stratospheric AOD change in HadGEM2-ES is higher than the prescribed value in the MIROC-based models, which may be a primary cause of the strongest SAI-induced cooling over China in HadGEM2-ES in this study. Conversely, deficits in column-integrated water vapor over China caused by SAI occur in all models, with magnitudes of −2.28 to −0.88 kg m^{-2} in summer and −0.62 to −0.27 kg m^{-2} in winter. This reduction contributes to a decrease in atmospheric absorption of solar radiation, leading to the increase in SW_{WV} (Fig. 10a–10f).

In addition to the SW_{SRM} and SW_{WV}, SW_C and SW_{SA} also play important roles in surface SW changes. The results indicate that changes in SW_C and SW_{SA} mainly determine the spatial pattern of net surface SW changes caused by SAI over China. The SW_C changes, which are the same as the changes in SW_CRE, are discussed in Sect. 4.2. The SW_{SA} changes are closely related to land surface conditions. The SAI-induced increase in surface albedo in G4 leads to negative SW_{SA} change over China (Fig. 10g–10l). In summer, the values of increased surface albedo are relatively small, with regional averages of 0.001 in HadGEM2-ES and 0.002 in MIROC-based models. A significantly increased surface albedo of up to 0.026 occurs in the Tibetan Plateau in MIROC-based models, which leads to decreased surface SW_CS and contributes to surface cooling. The regionally averaged increases in surface albedo range from 0.005 to 0.014 in winter. In addition, the aforementioned abnormal warming seen over the source region of the Yellow River and the Sichuan Basin in MIROC-ESM is also closely related to the decreased surface albedo (Fig. 10k). Considering surface albedo can be reasonably described as a linear function of snow cover fraction (e.g., Qu and Hall, 2007; Li et al., 2016), we further investigate the spatial pattern of differences in snow cover fraction in MIROC-ESM, and find that matches with surface albedo changes over China (Fig. S5; note that model data are not available for the other two models). It suggests that the SAI-induced surface albedo increase due to enlarged snow cover fraction gives rise to net surface SW decrease over China, which in turn has a positive feedback on surface cooling.

5 Conclusions and discussion

We analyze the surface air temperature response to SAI forcing over China based on the simulations ~~from~~of the G4 experiment and RCP4.5 scenario ~~in three models (~~by using six GCMs (BNU-ESM, CanESM2, CNRM-ESM1, HadGEM2-ES, MIROC-ESM and MIROC-ESM-CHEM). We also discuss the physical processes involved in the temperature response from a surface energy budget perspective. The main conclusions are summarized as follows.

(1) ~~The three~~All selected models can well reproduce the present climatological surface air temperature over China in both summer and winter. ~~The cooling effect caused by~~Although the SAI in the G4 experiment ~~cannot return~~leads to a surface cooling over China, the climatological temperature ~~over China under RCP4.5 to~~in G4 is still higher than the present level~~ but can delay warming for several years. Although the SAI-induced temperature differences between the G4 and RCP4.5 simulations are negative over China during~~. During the simulation period of 2030–2069, ~~the cooling effect varies among models, regions and seasons.~~ SAI leads to a national-scale cooling over China in all models. Regionally, the multi-model mean cooling is 0.64°C in summer and 0.80°C in winter, respectively. The SAI-induced temperature change varies among models, regions and seasons.

(2) The decomposition of temperature change based on the surface energy budget indicates that the SAI-induced surface cooling over China is dominated by the robust decrease in downward clear-sky radiation fluxes (particularly in downward clear-sky longwave radiation flux), and associated with the changes in cloud effective forcing and surface albedo feedback. The shortwave radiative effect of clouds and the surface albedo feedback determine the spatial pattern of temperature change, which are somewhat model-dependent and display a level of regional and seasonal discrepancies.~~The regionally averaged surface radiation changes over China indicate that both the SAI-induced decreases in net surface SW and LW, except for the increased LW in winter in HadGEM2-ES, contribute to the surface cooling in all three models. In response to the SAI forcing, the spatial patterns of temperature changes over China are mainly induced by SW changes. In summer, the strong cooling in HadGEM2-ES and MIROC-ESM is mainly due to the decreased SW_CRE caused by the cloud cover decrease. The strong surface cooling over the Tibetan Plateau in MIROC-ESM-CHEM is related to the decreased SW_CS. In winter, the strong cooling in all three models, together with the abnormal warming in MIROC-ESM, is related to changes in SW_CS.~~

(3) Under SAI forcing, the decreased downward clear-sky longwave radiation is mainly due to the decreased tropospheric temperature and water vapor amount, and the decreased downward clear-sky shortwave radiation is mainly contributed by the aerosol scattering effect over China. The decreased latent heat flux generally reduces the cloud cover over China, but the change in summer cloud cover is closely associated with the anomalous tropospheric moisture flux convergence. The negative surface albedo feedback related to increased snow cover fraction also amplifies the surface cooling, especially over the Tibetan Plateau in summer, and over northwestern and central China in winter. ~~The net surface SW decomposition shows that the increased SW_{SRM} and SW_{SA} and the decreased SW_{WV} and SW_{C} have positive and negative contributions to the decrease in net surface SW over China, respectively. Generally, SW_{SRM} decreases and SW_{WV} increases in both summer and winter, which are related to the increased stratospheric AOD and decreased column-integrated water vapor, respectively. The SW_{C} and SW_{SA} changes mainly determine the spatial patterns of SW changes due to SAI forcing. Moreover, both the strong summer cooling over the Tibetan Plateau in MIROC-ESM-CHEM and the abnormal winter warming in MIROC-ESM are related to the surface albedo changes.~~ The results above are summarized schematically in Fig. 12~~1~~.

Finally, note that equatorial~~Equatorial~~ stratospheric sulfate aerosol geoengineering can induce global cooling through the transport of Brewer-Dobson circulation, and also leads to regional inequities in the temperature response due to the complicated processes of aerosol microphysics and stratospheric transport (Kravitz et al., 2019). This means that some areas will face more severe climatic disasters if this kind of geoengineering is implemented. To solve this issue, certain SAI experiments based on the ~~regional~~ injection ~~method are~~at multiple locations have been proposed, such as the stratospheric aerosol geoengineering large ensemble project (GLENS) using CESM1(WACCM) (Tilmes et al., 2018). In addition, the uncertainty of the regional climate response to SAI is closely related to the reliability of the models (Irvine et al., 2016). It ~~is~~has been indicated that the CMIP6 GCMs perform better in simulating the temperature over China than their CMIP5 ~~GCMs~~counterparts (Jiang et al., 2020). Therefore, the climate response to SAI geoengineering over China based on state-of-the-art GCM experiments merits further study.

Code and data availability. The dataset used in this study can be accessed with the following links: https://esgf-node.llnl.gov/search/cmip5/.

Author contributions. Dabang Jiang and Zhaochen Liu designed and performed the research. Zhaochen Liu and Xianmei Lang ~~analysed~~analyzed the data. Zhaochen Liu and Dabang Jiang wrote the manuscript. All authors contributed to this study.

Competing interests. The authors declare no competing interests.

Acknowledgments. We sincerely thank the four anonymous reviewers for their insightful comments and suggestions to improve this manuscript. We acknowledge the Geoengineering Model Intercomparison Project Steering Committee and the World Climate Research Program's Working Group on Coupled Modelling. We also thank the climate modelling groups for producing their model outputs. ~~For the MIROC-based models, we~~We thank Helene Muri, Ji Duoying, John Moore and Toshihiro Nemoto for ~~his~~their help in downloading the GeoMIP outputs. This work was supported by the National Natural Science Foundation of China (42175031 and 41991284)~~ and the Second Tibetan Plateau Scientific Expedition and Research Program (2019QZKK0101)~~.

References

~~Andrews, T., Forster, P. M., and Gregory, J. M.: A surface energy perspective on climate change, J. Clim., 22, 2557–2570, https://doi.org/10.1175/2008JCLI2759.1, 2009.~~

Arora, V. K., Scinocca, J. F., Boer, G. J., Christian, J. R., Denman, K. L., Flato, G. M., Kharin, V. V., Lee, W. G., and Merryfield, W. J.: Carbon emission limits required to satisfy future representative concentration pathways of greenhouse gases, Geophys. Res. Lett., 38, L05805, https://doi.org/10.1029/2010GL046270, 2011.

Bala, G., Duffy, P. B., and Taylor, K. E.: Impact of geoengineering schemes on the global hydrological cycle, Proc. Natl. Acad. Sci. U. S. A., 105, 7664–7669, https://doi.org/10.1073/pnas.0711648105, 2008.

Bellouin, N., Rae, J., Jones, A., Johnson, C., Haywood, J., and Boucher, O.: Aerosol forcing in the Climate Model Intercomparison Project (CMIP5) simulations by HadGEM2-ES and the role of ammonium nitrate, J. Geophys. Res., 116, D20206, https://doi.org/10.1029/2011JD016074, 2011.

Bluth, G. J., Doiron, S. D., Schnetzler, C. C., Krueger, A. J., and Walter, L. S.: Global tracking of the

SO_2 clouds from the June, 1991 Mount Pinatubo eruptions, Geophy. Res. Lett., 19, 151–154, https://doi.org/10.1029/91GL02792, 1992.

~~Boer, G. J.: Climate change and the regulation of the surface moisture and energy budgets,Dyn., 8, 225–239, 1993.~~

Budyko, M. I.: Climatic Changes, American Geophysical Union, Washington, DC, 244 pp., https://doi.org/10.1029/SP010, 1977.

Caldeira, K., Bala, G., and Cao, L.: The science of geoengineering. Annu. Rev. Earth Planet. Sci., 41, 231–256, https://doi.org/10.1146/annurev-earth-042711-105548, 2013.

Cao, L., Gao, C. C., and Zhao, L. Y.: Geoengineering: Basic science and ongoing research efforts in China, Adv. Clim. Chang. Res., 6, 188–196, http://dx.doi.org/10.1016/j.accre.2015.11.002, 2015.

Collins, W. J., Bellouin, N., Doutriaux-Boucher, M., Gedney, N., Halloran, P., Hinton, T., Hughes, J., Jones, C. D., Joshi, M., Liddicoat, S., Martin, G., O'Connor, F., Rae, J., Senior, C., Sitch, S., Totterdell, I., Wiltshire, A., and Woodward, S.: Development and evaluation of an earth-system model – HadGEM2, Geosci. Model Dev., 4, 1051–1075, https://doi.org/10.5194/gmd-4-1051-2011, 2011.

Crutzen, P. J.: Albedo enhancement by stratospheric sulfur injections: A contribution to resolve a policy dilemma? Clim. Change, 77, 211–220, https://doi.org/10.1007/s10584-006-9101-y, 2006.

Duan, L., Cao, L., Bala, G., and Caldeira, K.: Climate response to pulse versus sustained stratospheric aerosol forcing, Geophys. Res. Lett., 46, 8976–8984, https://doi.org/10.1029/2019GL083701, 2019.

Donohoe, A., and Battisti, D. S.: Atmospheric and surface contributions to planetary albedo, J. Clim., 24, 4402–4418, https://doi.org/10.1175/2011JCLI3946.1, 2011.

Eastham, S. D., Weisenstein, D. K., Keith, D. W., and Barrett, S. R.: Quantifying the impact of sulfate geoengineering on mortality from air quality and UV-B exposure, Atmos. Environ., 187, 424–434, https://doi.org/10.1016/j.atmosenv.2018.05.047, 2018.

Gong, T., Feldstein, S., and Lee, S.: The role of downward infrared radiation in the recent Arctic winter warming trend, J. Clim., 30, 4937–4949, https://doi.org/10.1175/JCLI-D-16-0180.1, 2017.

Irvine, P. J., Kravitz, B., Lawrence, M. G., and Muri, H.: An overview of the Earth system science of solar geoengineering, Wiley Interdiscip. Rev.-Clim. Chang., 7, 815–833, https://doi.org/10.1002/wcc.423, 2016.

Irvine, P. J., Emanuel, K., He, J., Horowitz, L. W., Vecchi, G., and Keith, D.: Halving warming with idealized solar geoengineering moderates key climate hazards, Nat. Clim. Change, 9, 295–299, 2019.

Jarvis, A.: The magnitudes and timescales of global mean surface temperature feedbacks in climate models, Earth Syst. Dynam., 2, 213–221, https://doi.org/10.5194/esd-2-213-2011, 2011.

Ji, D., Wang, L., Feng, J., Wu, Q., Cheng, H., Zhang, Q., Yang, J., Dong, W., Dai, Y., Gong, D., Zhang, R. H., Wang, X., Liu, J., Moore, J. C., Chen, D., and Zhou, M.: Description and basic evaluation of Beijing Normal University Earth System Model (BNU-ESM) version 1, Geosci. Model Dev., 7, 2039–2064, https://doi.org/10.5194/gmd-7-2039-2014, 2014.

Ji, D., Fang, S., Curry, C., Kashimura, H., Watanabe, S., Cole, J. N., Lenton, A., Muri, H., Kravitz, B., and Moore, J.: Extreme temperature and precipitation response to solar dimming and stratospheric aerosol geoengineering, Atmos. Chem. Phys., 18, 10133–10156, https://doi.org/10.5194/acp-18-10133-2018, 2018.

Jiang, D., Tian, Z., and Lang, X.: Reliability of climate models for China through the IPCC third to fifth assessment reports, Int. J. Climatol., 36, 1114–1133, https://doi.org/10.1002/joc.4406, 2016.

Jiang, D., Hu, D., Tian, Z., and Lang, X.: Differences between CMIP6 and CMIP5 models in simulating climate over China and the East Asian monsoon, Adv. Atmos. Sci., 37, 1102–1118, https://doi.org/10.1007/s00376-020-2034-y, 2020.

Jones, A., Haywood, J. M., Alterskjær, K., Boucher, O., Cole, J. N., Curry, S., Charles, L., Irvine, P. J., Ji, D., Kravitz, B., Egill-Kristjánsson, J., Moore, J. C., Niemeier, U., Robock, A., Schmidt, H., Singh, B., Tilmes, S., Watanabe, S., and Yoon, J.-H.: The impact of abrupt suspension of solar radiation management (termination effect) in experiment G2 of the Geoengineering Model Intercomparison Project (GeoMIP), J. Geophys. Res.-Atmos., 118, 9743–9752, https://doi.org/10.1002/jgrd.50762, 2013.

Jones, A. C., Hawcroft, M. K., Haywood, J. M., Jones, A., Guo, X., and Moore, J. C.: Regional climate impacts of stabilizing global warming at 1.5 K using solar geoengineering, Earths Future, 6, 230–251, https://doi.org/10.1002/2017EF000720, 2018.

Kashimura, H., Abe, M., Watanabe, S., Sekiya, T., Ji, D., Moore, J. C., Cole, J. N., and Kravitz, B.: Shortwave radiative forcing, rapid adjustment, and feedback to the surface by sulfate geoengineering: Analysis of the Geoengineering Model Intercomparison Project G4 scenario,

637 Atmos. Chem. Phys., 17, 3339–3356, https://doi.org/10.5194/acp-17-3339-2017, 2017.
638 Kravitz, B., Robock, A., Boucher, O., Schmidt, H., Taylor, K. E., Stenchikov, G., and Schulz, M.: The
639 Geoengineering Model Intercomparison Project (GeoMIP), Atmos. Sci. Lett., 12, 162–167,
640 https://doi.org/10.1002/asl.316, 2011.
641 Kravitz, B., Robock, A., Forster, P. M., Haywood, J. M., Lawrence, M. G., and Schmidt, H.: An
642 overview of the Geoengineering Model Intercomparison Project (GeoMIP), J. Geophys. Res.-
643 Atmos., 118, 13103–13107, https://doi.org/10.1002/2013JD020569, 2013a.
644 Kravitz, B., Rasch, P. J., Forster, P. M., Andrews, T., Cole, J. N., Irvine, P. J., Ji, D., Kristjánsson, J.,
645 Moore, J. C., Muri, H., Niemeier, U., Robock, A., Singh, B., Tilmes, S., Watanabe, S., and Yoon,
646 J.-H.: An energetic perspective on hydrological cycle changes in the Geoengineering Model
647 Intercomparison Project, J. Geophys. Res.-Atmos., 118, 13087–13102,
648 https://doi.org/10.1002/2013JD020502, 2013b.
649 Kravitz, B., MacMartin, D. G., Robock, A., Rasch, P. J., Ricke, K. L., Cole, J. N., Curry, C. L., Irvine,
650 P. J., Ji, D., Keith, D. W., Kristjánsson, J. E., Moore, J. C., Muri, H., Singh, B., Tilmes, S.,
651 Watanabe, S., Yang, S., and Yoon, J. H.: A multi-model assessment of regional climate disparities
652 caused by solar geoengineering, Environ. Res. Lett., 9, 074013, https://doi.org/10.1088/1748-
653 9326/9/7/074013, 2014.
654 Kravitz, B., Robock, A., Tilmes, S., Boucher, O., English, J. M., Irvine, P. J., Jones, A., Lawrence, M.
655 G., MacCracken, M., Muri, H., Moore, J. C., Niemeier, U., Phipps, S. J., Sillmann, J., Storelvmo,
656 T., Wang, H., and Watanabe, S.: The Geoengineering Model Intercomparison Project Phase 6
657 (GeoMIP6): simulation design and preliminary results, Geosci. Model Dev., 8, 3379–3392,
658 https://doi.org/10.5194/gmd-8-3379-2015, 2015.
659 Kravitz, B., MacMartin, D. G., Tilmes, S., Richter, J. H., Mills, M. J., Cheng, W., Dagon, K., Glanville,
660 A. S., Lamarque, J.-F., Simpson, I. R., Tribbia, J., and Vitt, F.: Comparing surface and
661 stratospheric impacts of geoengineering with different SO_2 injection strategies, J. Geophys. Res.-
662 Atmos., 124, 7900–7918, https://doi.org/10.1029/2019JD030329, 2019.
663 Latham, J.: Control of global warming? Nature, 347, 339–340, https://doi.org/10.1038/347339b0, 1990.
664 Li, Y., Wang, T., Zeng, Z., Peng, S., Lian, X., and Piao, S.: Evaluating biases in simulated land surface
665 albedo from CMIP5 global climate models, J. Geophys. Res.-Atmos., 121, 6178–6190,
666 https://doi.org/10.1002/2016JD024774, 2016.

Lu, J., and Cai, M.: Seasonality of polar surface warming amplification in climate simulations, Geophys. Res. Lett., 36, L16704, https://doi.org/10.1029/2009GL040133, 2009.

Matthews, H. D., and Caldeira, K.: Transient climate–carbon simulations of planetary geoengineering, Proc. Natl. Acad. Sci. U. S. A., 104, 9949–9954, https://doi.org/10.1073/pnas.0700419104, 2007.

Mitchell, D. L., and Finnegan, W.: Modification of cirrus clouds to reduce global warming, Environ. Res. Lett., 4, 045102, https://doi.org/10.1088/1748-9326/4/4/045102, 2009.

Phipps, S. J., Rotstayn, L. D., Gordon, H. B., Roberts, J. L., Hirst, A. C., and Budd, W. F.: The CSIRO Mk3L climate system model version 1.0 – Part 1: Description and evaluation, Geosci. Model Dev., 4, 483–509, https://doi.org/10.5194/gmd-4-483-2011, 2011.

Qu, X., and Hall, A.: What controls the strength of snow-albedo feedback? J. Clim., 20, 3971–3981, https://doi.org/10.1175/JCLI4186.1, 2007.

Raible, C. C., Brönnimann, S., Auchmann, R., Brohan, P., Frölicher, T. L., Graf, H. F., Jones, P., Luterbacher, J., Muthers, S., Neukom, R., Robock, A., Self, S., Sudrajat, A., Timmreck, C., and Wegmann, M.: Tambora 1815 as a test case for high impact volcanic eruptions: Earth system effects, Wiley Interdiscip. Rev.-Clim. Chang., 7, 569–589, https://doi.org/10.1002/wcc.407, 2016.

Rasch, P. J., Crutzen, P. J., and Coleman, D. B.: Exploring the geoengineering of climate using stratospheric sulfate aerosols: The role of particle size, Geophys. Res. Lett., 35, L02809, https://doi.org/10.1029/2007GL032179, 2008.

Ricke, K. L., Moreno-Cruz, J. B., and Caldeira, K.: Strategic incentives for climate geoengineering coalitions to exclude broad participation, Environ. Res. Lett., 8, 014021, https://doi.org/10.1088/1748-9326/8/1/014021, 2013.

Robiou du Pont, Y., and Meinshausen, M.: Warming assessment of the bottom-up Paris Agreement emissions pledges, Nat. Commun., 9, 4810, https://doi.org/10.1038/s41467-018-07223-9, 2018.

Robock, A., Oman, L., and Stenchikov, G. L.: Regional climate responses to geoengineering with tropical and Arctic SO_2 injections, J. Geophys. Res., 113, D16, https://doi.org/10.1029/2008JD010050, 2008.

Robock, A.: Stratospheric aerosol geoengineering, AIP Conf. Proc., 1652, 183–197, https://doi.org/10.1063/1.4916181, 2015.

Russotto, R. D., and Ackerman, T. P.: Energy transport, polar amplification, and ITCZ shifts in the GeoMIP G1 ensemble, Atmos. 2287–2305, https://doi.org/10.5194/acp-18-2287-2018, 2018.

Sato, M.: Forcings in GISS climate model: Stratospheric aerosol optical thickness, available at: https://data.giss.nasa.gov/modelforce/strataer/, 2006. (last access: April 2021)

Schmidt, H., Alterskjær, K., Bou Karam, D., Boucher, O., Jones, A., Kristjánsson, J. E., Niemeier, U., Schulz, M., Aaheim, A., Benduhn, F., Lawrence, M., and Timmreck, C.: Solar irradiance reduction to counteract radiative forcing from a quadrupling of CO_2: Climate responses simulated by four earth system models, Earth Syst. Dynam., 3, 63–78, https://doi.org/10.5194/esd-3-63-2012, 2012.

Seifritz, W.: Mirrors to halt global warming, Nature, 340, 603, https://doi.org/10.1038/340603a0, 1989.

~~Shepherd, J. G.: Geoengineering the climate: Science, governance and uncertainty, Royal Society, London, 2009.~~

Séférian, R., Delire, C., Decharme, B., Voldoire, A., David, S. Y. M., Chevallier, M., Saint-Martin, D., Aumont, O., Calvet, J.-C., Carrer, D., Douville, H., Franchistéguy, L., Joetzjer, E., and Sénési, S.: Development and evaluation of CNRM Earth system model – CNRM-ESM1, Geosci. Model Dev., 9, 1423–1453, https://doi.org/10.5194/gmd-9-1423-2016, 2016.

Sudo, K., Takahashi, M., Kurokawa, J., and Akimoto, H.: CHASER: A global chemical model of the troposphere: 1. Model description, J. Geophys. Res., 107, 4339, https://doi.org/10.1029/2001JD001113, 2002.

Sun, W., Wang, B., Chen, D., Gao, C., Lu, G., and Liu, J.: Global monsoon response to tropical and Arctic stratospheric aerosol injection, Clim. Dyn., 55, 2107–2121, https://doi.org/10.1007/s00382-020-05371-7, 2020.

Taylor, K. E.: Summarizing multiple aspects of model performance in a single diagram, J. Geophys. Res.-Atmos., 106, 7183–7192, https://doi.org/10.1029/2000JD900719, 2001.

Taylor, K. E., Stouffer, R. J., and Meehl, G. A.: An overview of CMIP5 and the experiment design, Bull. Amer. Meteorol. Soc., 93, 485–498, https://doi.org/10.1175/BAMS-D-11-00094.1, 2012.

Tilmes, S., Müller, R., and Salawitch, R.: The sensitivity of polar ozone depletion to proposed geoengineering schemes, Science, 320, 1201–1204, https://doi.org/10.1126/science.1153966, 2008.

Tilmes, S., Fasullo, J., Lamarque, J. F., Marsh, D. R., Mills, M., Alterskjær, K., Muri, H., Kristjánsson, J. E., Boucher, O., Schulz, M., Cole, J. N. S., Curry, C. L., Jones, A., Haywood, J., Irvine, P. J., Ji, D., Moore, J. C., Karam, D. B., Kravitz, B., Rasch, P. J., Singh, B., Yoon, J.-H., Niemeier, U.,

Schmidt, H., Robock, A., Yang, S., and Watanabe, S.: The hydrological impact of geoengineering in the Geoengineering Model Intercomparison Project (GeoMIP), J. Geophys. Res.-Atmos., 118, 11036–11058, https://doi.org/10.1002/jgrd.50868, 2013.

Tilmes, S., Richter, J. H., Kravitz, B., MacMartin, D. G., Mills, M. J., Simpson, I. R., Glanville, A. S., Fasullo, J. T., Phillips, A. S., Lamarque, J.-F., Tribbia, J., Edwards, J., Mickelson, S., and Ghosh, S.: CESM1 (WACCM) stratospheric aerosol geoengineering large ensemble project, Bull. Amer. Meteorol. Soc., 99, 2361–2371, https://doi.org/10.1175/BAMS-D-17-0267.1, 2018.

Trenberth, K. E., and Dai, A.: Effects of Mount Pinatubo volcanic eruption on the hydrological cycle as an analog of geoengineering, Geophys. Res. Lett., 34, 1438–1442, https://doi.org/10.1029/2007GL030524, 2007.

United Nations Environment Programme.: Emissions Gap Report 2020, UNEP, Nairobi, 2020.

Visioni, D., Pitari, G., di Genova, G., Tilmes, S., and Cionni, I.: Upper tropospheric ice sensitivity to sulfate geoengineering, Atmos. Chem. Phys., 18, 14867–14887, https://doi.org/10.5194/acp-18-14867-2018, 2018.

Watanabe, S., Hajima, T., Sudo, K., Nagashima, T., Takemura, T., Okajima, H., Nozawa, T., Kawase, H., Abe, M., Yokohata, T., Ise, T., Sato, H., Kato, E., Takata, K., Emori, S., and Kawamiya, M.: MIROC-ESM 2010: Model description and basic results of CMIP5-20c3m experiments, Geosci. Model Dev., 4, 845–872, https://doi.org/10.5194/gmd-4-845-2011, 2011.

Wigley, T. M. L.: A combined mitigation/geoengineering approach to climate stabilization, Science, 314, 452–454, https://doi.org/10.1126/science.1131728, 2006.

Wu, J., and Gao, X.: A gridded daily observation dataset over China region and comparison with the other datasets, Chinese J. Geophy., 56, 1102–1111, https://doi.org/10.6038/cjg20130406, 2013. (in Chinese)

~~Yu, X., Moore, J. C., Cui, X., Rinke, A., Ji, D., Kravitz, B., and Yoon, J.-H.: Impacts, effectiveness and regional inequalities of the GeoMIP G1 to G4 solar radiation management scenarios, Glob. Planet. Change, 129, 10–22, https://doi.org/10.1016/j.gloplacha.2015.02.010, 2015.~~

753 **Table 1**. Main features ~~and references~~ of ~~three~~climate models used in this study.

Model	Atmospheric resolution (longitude, latitude, and vertical levels)	Ensemble number	Stratospheric aerosol	Reference
BNU-ESM	~2.8° × ~2.8°, L26	1	Prescribed	Ji et al., 2014
CanESM2	~2.8° × ~2.8°, L35	3	Uniform	Arora et al., 2011
CNRM-ESM1	~1.4° × ~1.4°, L31	2	Prescribed	Séférian et al., 2016
HadGEM2-ES	1.875° × 1.25°, L38	3	Generated from SO_2 injection	Collins et al., 2011
MIROC-ESM	~2.8° × ~2.8°, L80	1	Prescribed	Watanabe et al., 2011
MIROC-ESM-CHEM	~2.8° × ~2.8°, L80	1	Prescribed	Watanabe et al., 2011

754

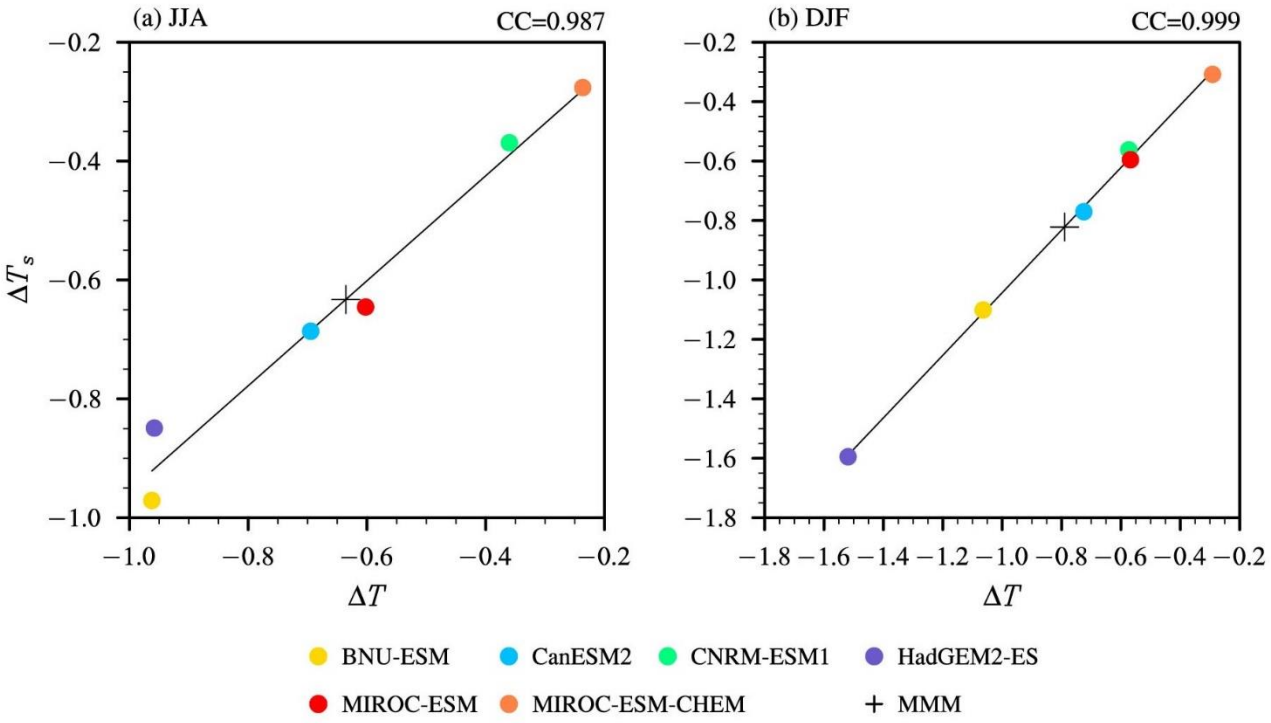

Figure 1. Scatter plots of relationship between changes in surface air temperature (T) and surface temperature (T_s) over China due to SAI forcing during the period of 2030–2069 in (a) summer (JJA) and (b) winter (DJF), and CC is their correlation coefficient. Scatters and cross represent individual models and their mean,~~Schematic illustration representing the impacts of SAI geoengineering on net shortwave radiation flux at the surface. The SW_{SRM}, SW_{WV}, SW_C, and SW_{SA} represent the changes in shortwave radiation at the surface caused by those in solar radiation modification strength, amount of atmospheric water vapor, cloudiness, and surface albedo,~~ respectively.

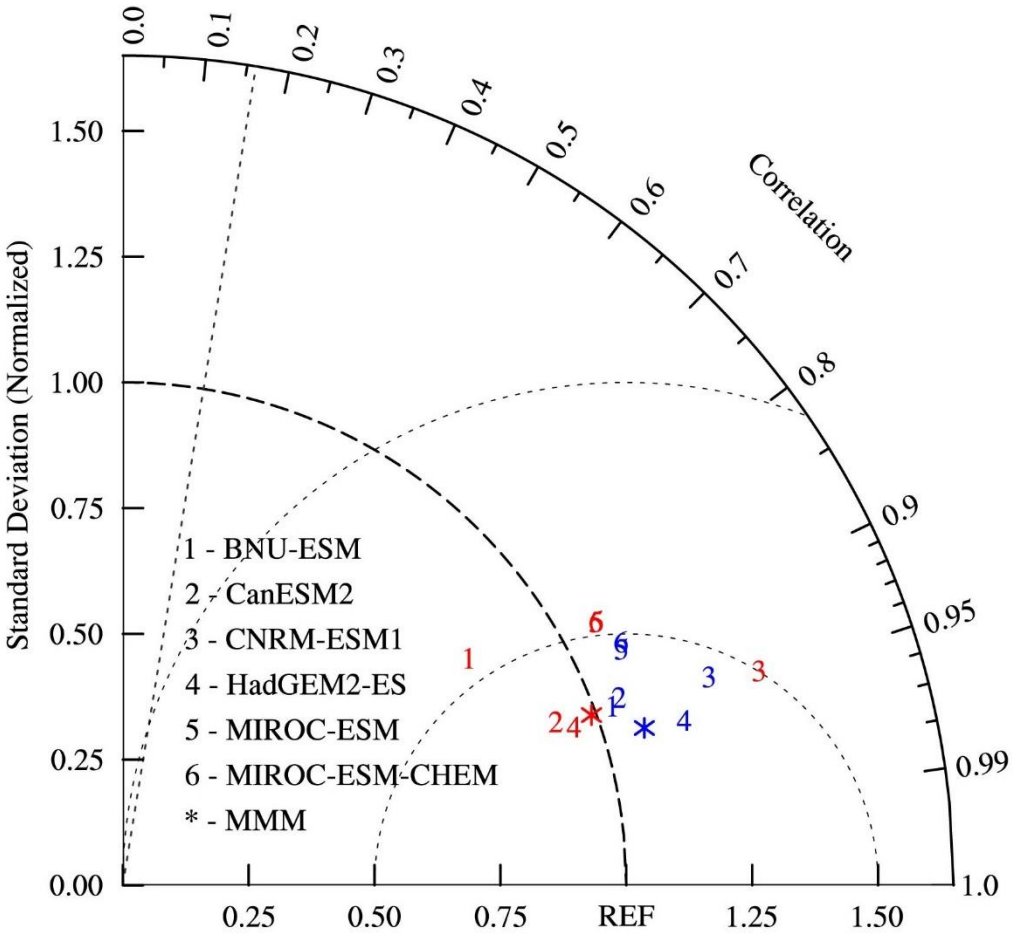

Figure 2. Taylor diagram of climatological ~~seasonal~~summer and winter temperatures over China between the historical simulations in selected models and observation during the ~~present~~ period of 1986–2005. Numbers represent individual models~~.~~, and asterisks represent the multi-model mean. Red and blue represent summer and winter, respectively. The ~~oblique~~ dotted straight line shows the 99% confidence level determined from the two-tailed Student's *t*-test.

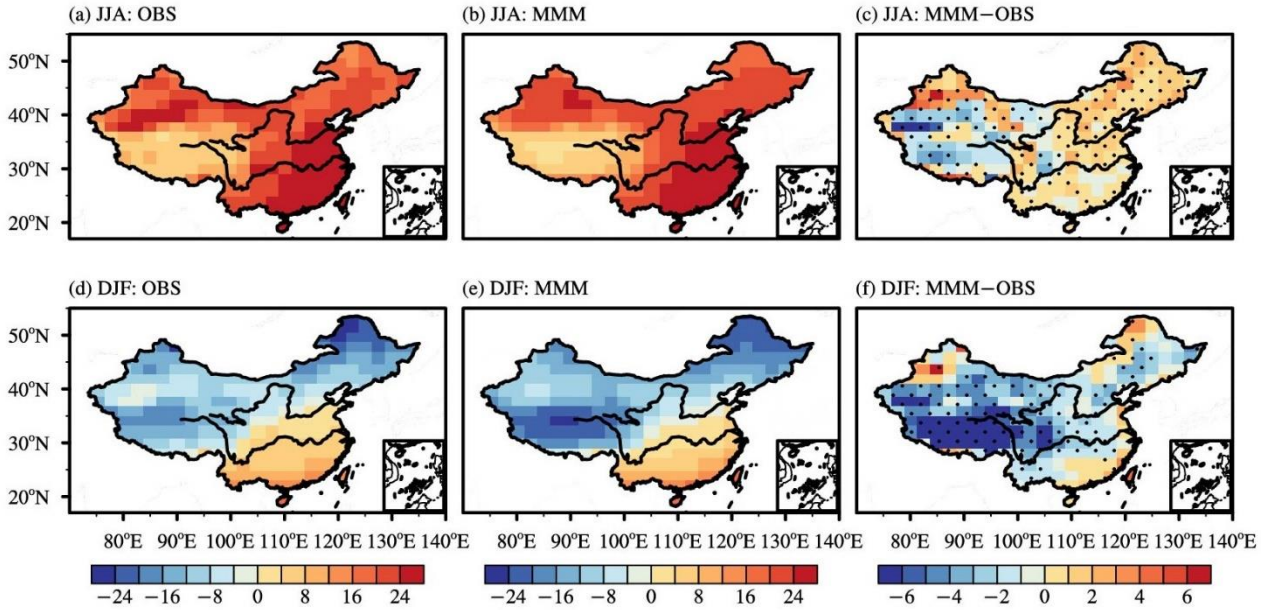

Figure 3. Spatial patterns of surface air temperature ~~biases~~climatology (units: °C) over China ~~between simulations in the historical experiment and~~ as obtained from observation (left column; OBS), the multi-model mean (middle column; MMM), and the difference between multi-model mean and observation (right column; MMM–OBS) during the ~~present~~ period of 1986–2005 in ~~(a–c)~~ summer (JJA) and ~~(d–f)~~ winter (DJF). ~~Numbers in parentheses represent regionally averaged values in China.~~The dots in the right column indicate areas where at least two-thirds of models share the same sign of the bias.

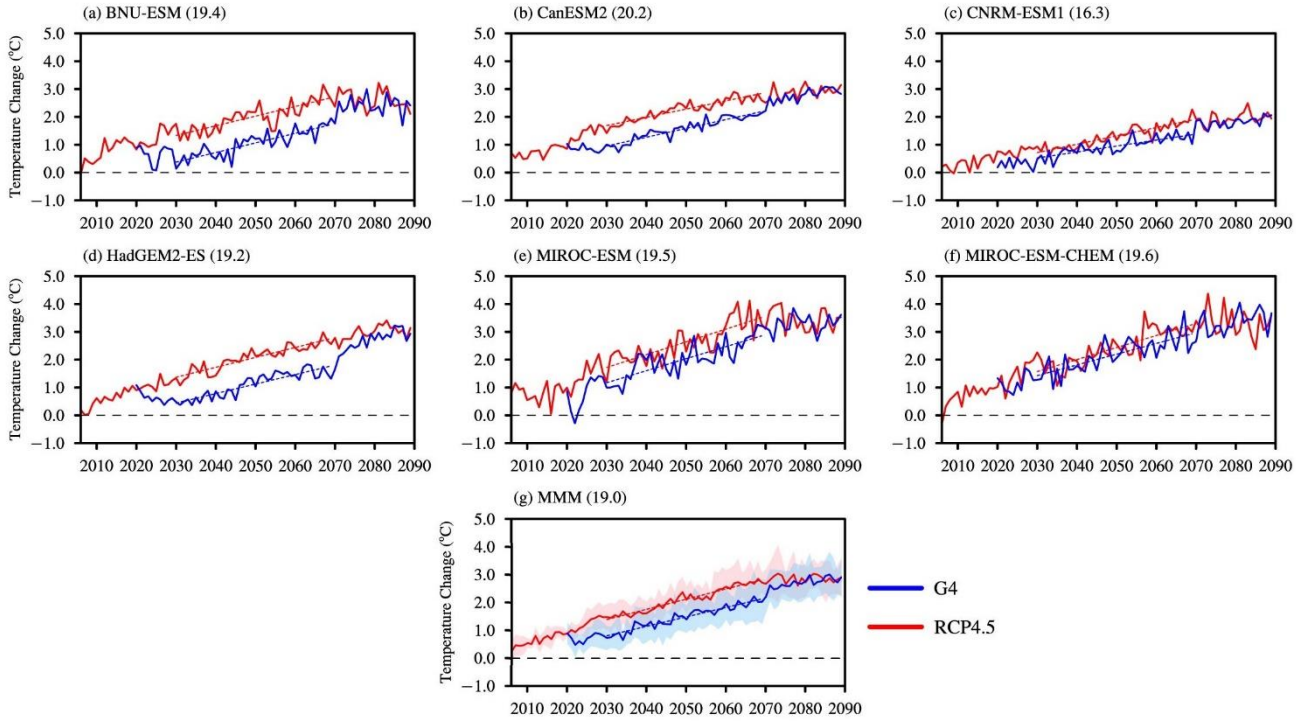

777

778 **Figure 4**. Time series of regionally averaged surface air temperature (units: °C) over China in the G4
779 experiment (solid blue lines) and RCP4.5 scenario (solid red lines) in summer ~~(JJA) and winter (DJF).~~.
780 The values are obtained by subtracting the present climatology (mean of 1986–2005; represented in
781 parentheses) in the historical experiment. Red and blue dashed lines represent the ~~Theil Sen~~linear
782 trends of G4 and RCP4.5 simulations during the period of 2030–2069, respectively. The multi-model
783 mean (MMM) is represented at the bottom, with the shading indicating one inter-model standard
784 deviation.

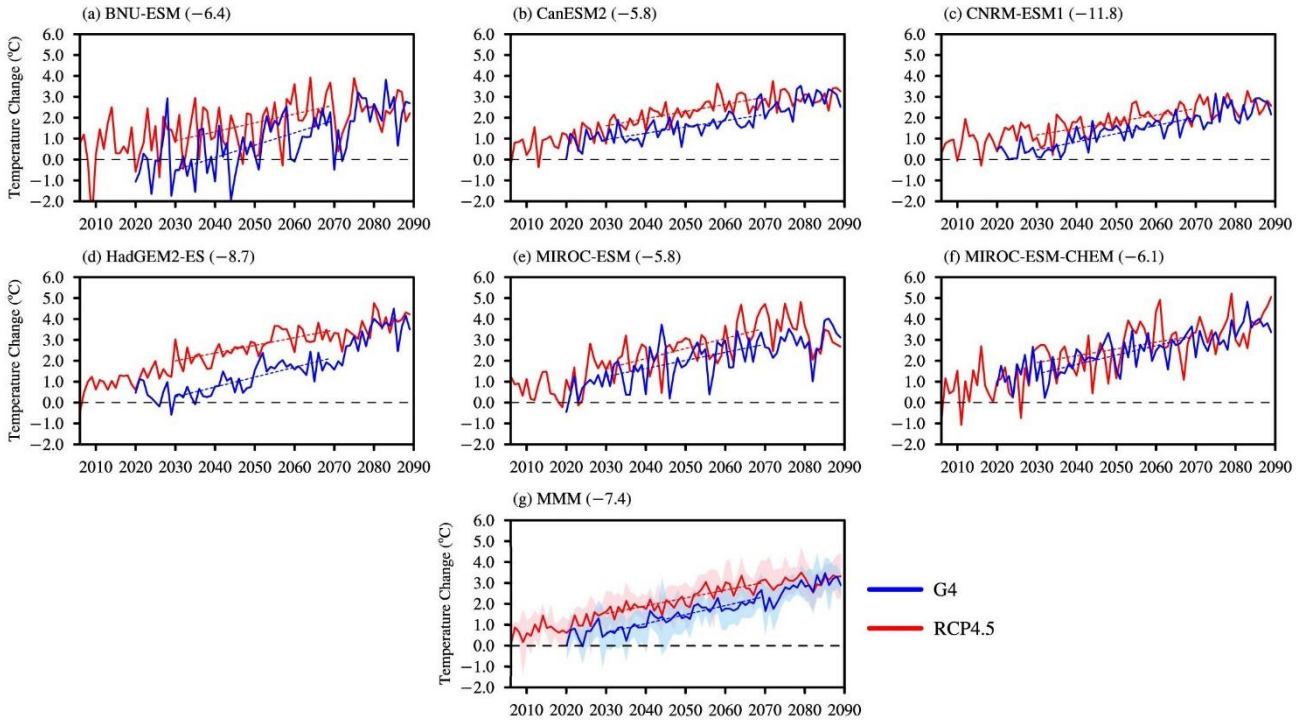

Figure 5. Same as Figure 4, but in winter.

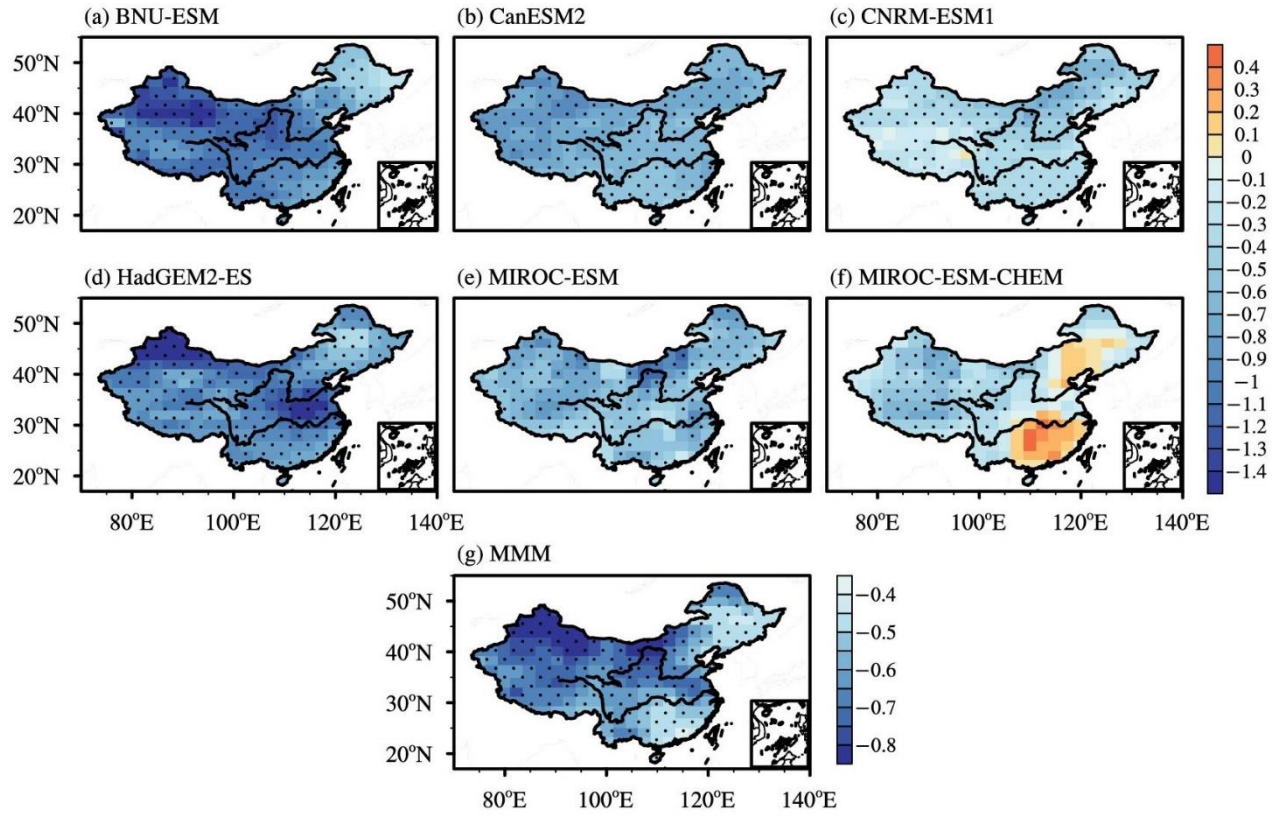

Figure 6. Spatial patterns of surface air temperature differences (units: °C) between G4 and RCP4.5 over China during the period of 2030–2069 in ~~(a–c)~~ summer ~~(JJA)~~for (a–f) individual models and (~~d–f) winter (DJF). Stippling indicates~~g) the multi-model mean. The dots in (a–f) indicate areas ~~that~~where are statistically significant at the 90% confidence level. The dots in (g) indicate areas where at least two-thirds of models share the same sign with the multi-model mean.

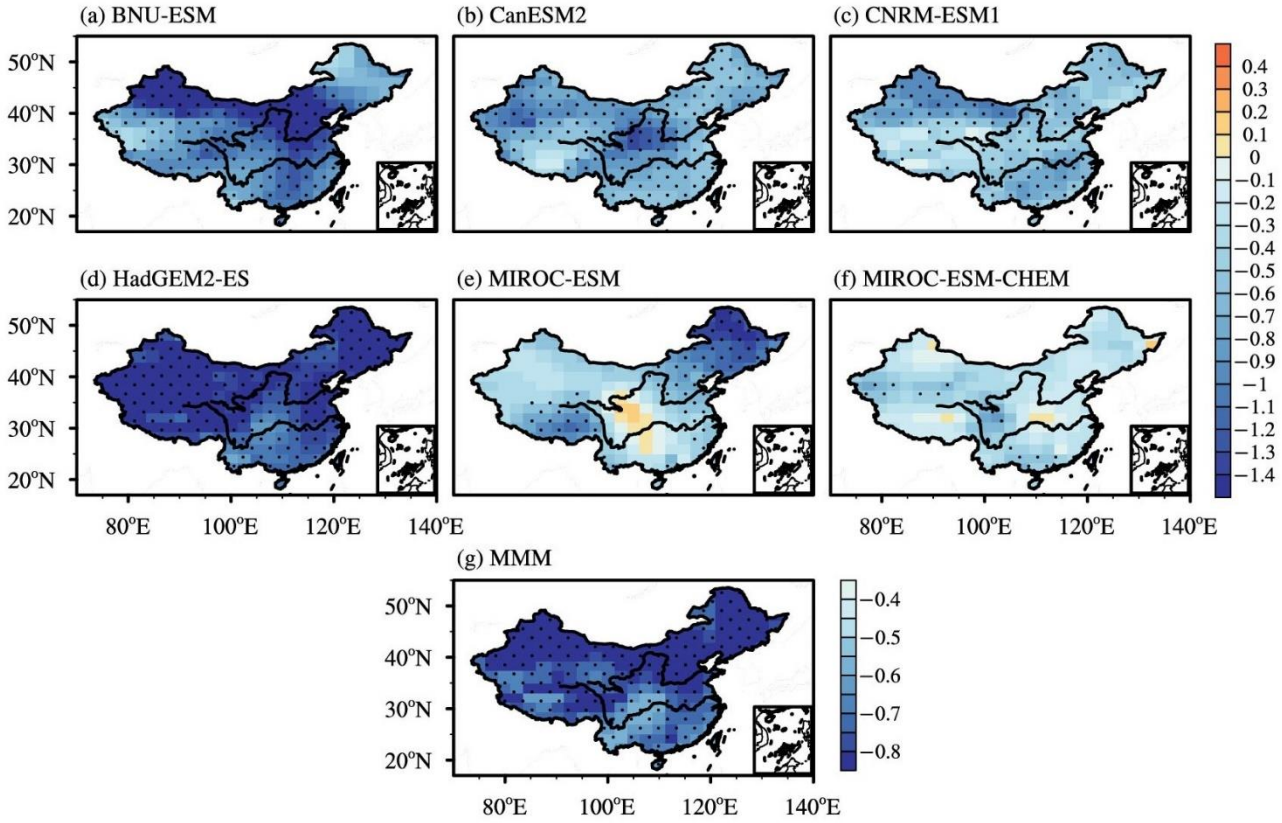

793

794 **Figure 7**. Same as Figure 6, but in winter.

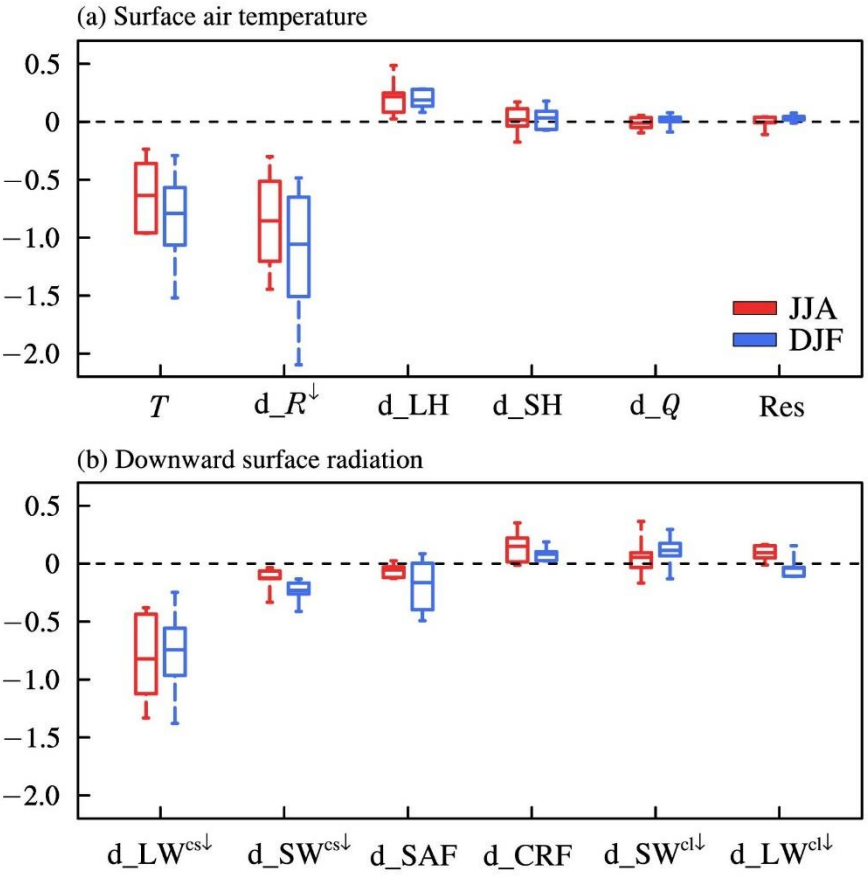

Figure 8~~6~~. Regionally averaged SAI-induced changes in surface air temperature (T~~,~~) and relevant terms over China during the period of 2030–2069 (units: °C~~), ~~). The terms include surface air temperature changes due to (a) downward net surface ~~shortwave (SW) and longwave (LW) ~~radiation~~,~~ change (d_$R^{\downarrow}$), surface latent ~~heat (~~(d_LH) and sensible (d_SH) heat flux changes, heat ~~(SH) flux,~~ storage change (d_Q), residual term change (Res), (b) downward clear-sky surface longwave (d_$LW^{cs\downarrow}$) and shortwave (d_$SW^{cs\downarrow}$) radiation changes, surface albedo feedback change (d_SAF) and surface cloud radiative forcing change (d_CRF; including shortwave (~~SW_CS~~d_$SW^{cl\downarrow}$) and longwave (~~LW_CS) radiation, and cloud radiative effect of shortwave (SW_CRE) and longwave (LW_CRE) in G4 compared to RCP4.5 over China during the period of 2030–2069. Red~~d_$LW^{cl\downarrow}$) forcing changes). The error bars represent minimum and maximum values, and the boxes represent interquartile ranges among models. The middle lines present multi-model means. The red and blue bars represent values in summer and winter, respectively. ~~Flux is in W m^{-2} with defining as downward positive.~~

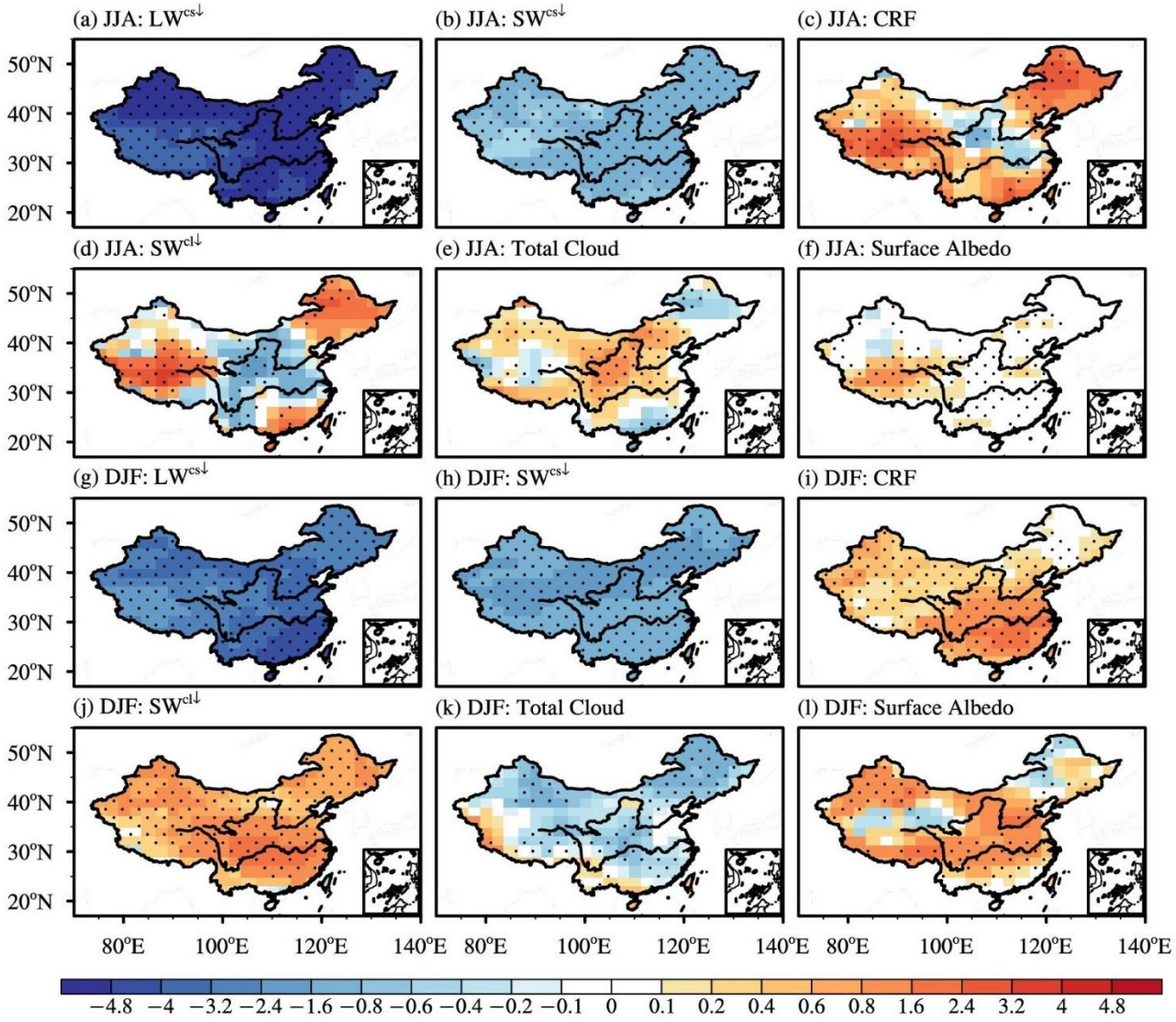

Figure ~~7~~9. Spatial patterns of differences between G4 and RCP4.5 over China for ~~HadGEM2-ES~~ the multi-model mean in summer (JJA) and winter (DJF): (a, ~~i) net~~g) downward clear-sky surface ~~shortwave~~longwave radiation (~~SW~~LW$^{cs\downarrow}$); (b, ~~j)~~h) downward clear-sky ~~net~~ surface shortwave radiation (~~SW_CS~~SW$^{cs\downarrow}$); (c, ~~k)~~i) surface cloud radiative ~~effect of shortwave (SW_CRE); (d, l~~forcing; (d, j) downward shortwave radiative effect of clouds (SW$^{cl\downarrow}$); (e, k) total cloud cover (units: %); (~~e, m) net surface longwave radiation (LW); (~~f, ~~n) clear-sky net surface longwave radiation (LW_CS); (g, o) cloud radiative effect of longwave (LW_CRE); (h, p) latent heat flux (LH)~~l) surface albedo (units: %) during the period of 2030–2069. Flux is in W m^{-2} ~~with defining as downward positive. Stippling indicates~~. The dots indicate areas ~~that are statistically significant at the 90% confidence level.~~where at least two-thirds of models share the same sign with the multi-model mean.

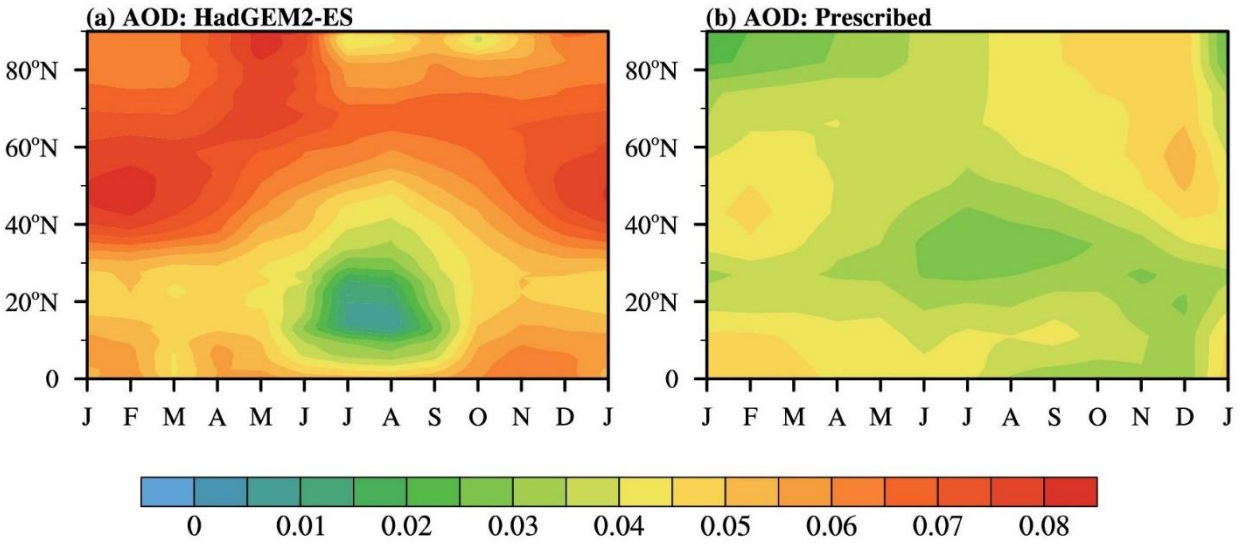

Figure 10~~9~~. Latitudinal distributions of the calculated (a, for HadGEM2-ES) and prescribed (b, for BNU-ESM, CNRM-ESM1, and the MIROC-~~ESM and MIROC-ESM-CHEM) stratospheric AOD~~based models) changes in SAOD at 550 nm caused by SAI in G4 experiment over the Northern Hemisphere during the period of 2030–2069.

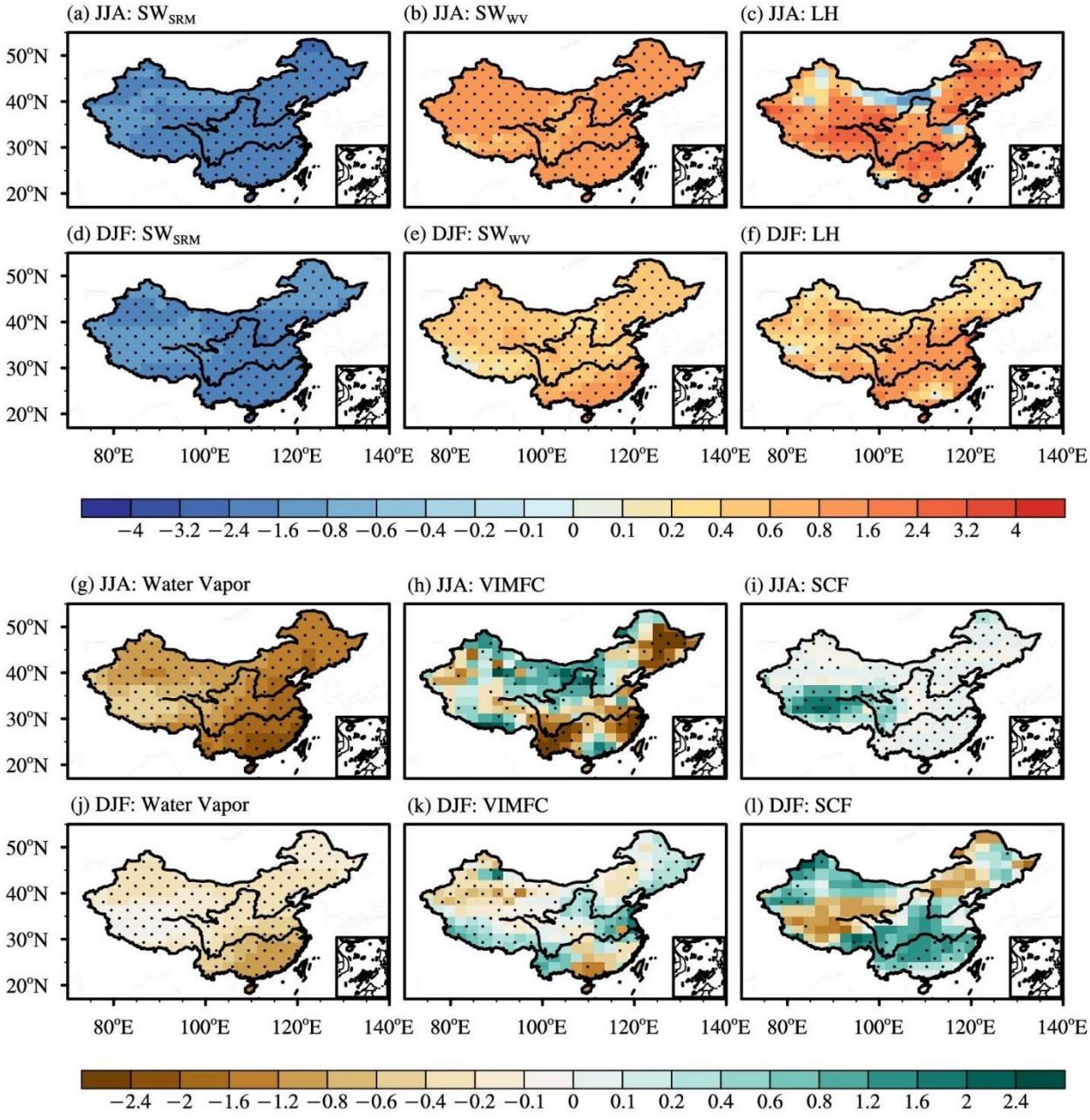

824

825 **Figure ~~10~~11**. Same as Figure ~~5~~9, but for the shortwave radiative effects of (a~~–f~~, d) solar radiation
826 scattering change (SW$_{SRM}$) and (b, e) atmospheric water vapor amount change (SW$_{WV}$), (c, f) latent
827 heat flux (LH), (g, j) column-integrated water vapor (units: kg m^{-2}~~) and (g–~~), (h, k) vertically integrated
828 moisture flux convergence (VIMFC; units: 0.1 mm d^{-1}), and (i, l) ~~surface albedo.~~snow cover fraction
829 (SCF; units: %). Flux is in W m^{-2} and defined positive downward.

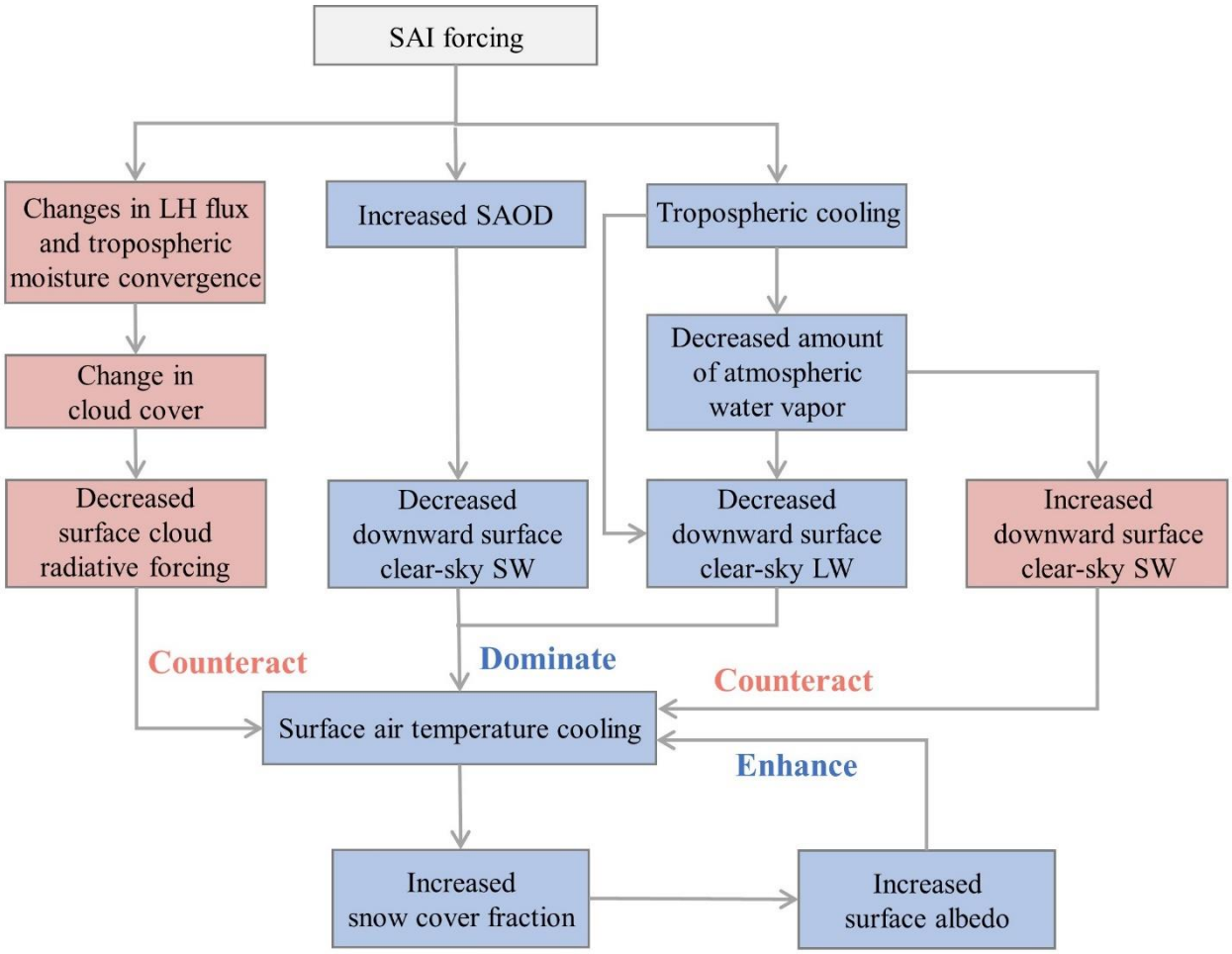

Figure ~~11~~12. Schematic diagram illustrating how the ~~related~~relevant physical processes impact the downward surface ~~SW~~radiation changes over China in response to the SAI forcing in the G4 experiment.